OPTICAL VORTEX RINGS IN ELLIPTIC GAUSSIAN BEAMS: TOPOLOGICAL REACTIONS AND CATASTROPHES

by

Zhamila Kulchukova

A Thesis Submitted to the Faculty of the

DEPARTMENT OF PHYSICS

In Partial Fulfillment of the Requirements
For the Degree of

MASTERS OF SCIENCE

In the School of Sciences and Humanities

NAZARBAYEV UNIVERSITY

2025

NAZARBAYEV UNIVERSITY, SCHOOL OF SCIENCES AND HUMANITIES

As members of the thesis committee, we certify that we have read the thesis prepared by Zhamila Kulchukova entitled

OPTICAL VORTEX RINGS IN ELLIPTIC GAUSSIAN BEAMS: TOPOLOGICAL REACTIONS AND CATASTROPHES

and recommend that it be accepted as fulfilling the thesis requirement for the degree of Masters of Science.

Final approval and acceptance of this thesis is contingent upon the candidate's submission of the final copies of the thesis to the Department of Physics.

I hereby certify that I have read this thesis prepared under my direction and recommend that it be accepted as fulfilling the thesis requirement.

_____ Date: May 1, 2025

Thesis Director: Anton Desyatnikov

ABSTRACT

Vortex rings are a fascinating subject in physics with a long history, offering insights into the intricate topology of the system. In this thesis, I investigate vortex rings generated by destructive interference of an elliptic Gaussian beam and a plane wave. The system can be replicated in optics laboratories using readily available equipment, but most importantly, it provides an assessable framework for studying complex topologies of vortex lines and even catastrophes.

The main results are split into two sections. In the first, I derive the governing equations of elliptic Gaussian beams. I explore various topological transformations of rings and examine how the underlying beam symmetries affect the dynamics of topological events. In the second, I analyze the effects of heightened ellipticity on the events and beam shapes, and investigate catastrophes occurring in the system.

The findings may provide deeper insights into the fine structure of light and potentially lay the foundation for understanding the mechanisms of spontaneous knotting of vortex lines.

TABLE OF CONTENTS

1 INTRODUCTION

The wave-like nature of the light is a well-established principle, thanks to centuries of theoretical and experimental work done proving so [1, 2]. This has laid the foundational knowledge for creating lasers, short for Light Amplification by Stimulated Emission of Radiation [3, 4]. The theoretical mechanism of stimulated emission was predicted by Einstein [5], and the device itself was realized by Maiman in 1960 [6]. Townes, Basov and Prokhorov [7–9], whose work was used as a blueprint for both laser and maser (laser in the microwave range), shared the 1964 Nobel Prize.

The laser is constructed via three main components: a power source for triggering excitation, an active gain medium that emits electromagnetic radiation after excitation, and the optical resonator in the form of mirrors attached to the ends of the gain medium. Current technologies allow for the generation of beams with various configurations, such as frequency, transverse profile, embedded caustics or special phase patterns, by manipulating the properties of the resonator and the active medium [10, 11].

Paraxial laser beams, which comply with the paraxial wave equation (2.5) and propagate at small angles w.r.t the optical axis [12], are of particular interest for this thesis. More specifically, elliptic Gaussian beams, whose intensity profile is described by the Gaussian distribution [13, 14] and transverse beam profile follow elliptic (quadrupole) symmetry [15]. An interesting property of the Gaussian beams that has captivated researchers is the presence of the Gouy phase anomaly or Gouy phase shift, due to which the beam acquires an additional $+\pi$ radians of phase as it propagates from the far field on one side of the focus to the other [16]. A detailed overview of the Gaussian beams will be provided in 2.1.

As we examine the subject of beam design, special attention should be paid to caustics. Caustics are physical manifestations of catastrophes; the latter are phenomena where small changes in the control parameters lead to dramatic changes in the system by causing equilibrium points of a potential function to appear or disappear. The zeros of first and subsequent higher-order derivatives of equilibrium points are called the "singularities" of the potential function. Mappings of such singularities in the domain of control parameters depict one of the established seven elementary catastrophes: fold, cusp, swallowtail, butterfly, hyperbolic umbilic, elliptic umbilic and parabolic umbilic. The theory was first introduced by Thom [17] and later developed with applications in physics by Arnold and Zeeman [18, 19]. A prominent example of catastrophes in optics is the rainbow line, which is a manifestation of a fold catastrophe [20].

In simpler terms, caustics are points of divergent intensity formed out of light reflecting or refracting off a curved surface; for example, speckles of light on the bottom of the pool. Unlike focused light, which gets destroyed if the focusing apparatus is deformed, caustics persist [21, 22]. Caustics in optics form in a similar way to rogue waves in oceans and can provide a good basis for studying other extreme wave phenomena [23, 24]. Rays can

model the general shape of and around caustics, however, in close proximity near the caustic itself, the geometrical optics principles are no longer valid. This is a consequence of complex diffraction effects, which remains a point of active research for decades [25–29]. Diffraction patterns of caustics formed by a water droplet and shaped into various families of catastrophes have been extensively studied, theoretically and experimentally [30–33], and special beams can be generated with specific types of catastrophes embedded in them [34–37].

An interesting observation is that by analyzing the diffraction pattern around the caustics, one may notice an arrangement of dark singular points with an undefined phase. Such points act as a skeleton supporting the caustic [26] as if trying to balance the extreme light with darkness. Furthermore, singularities in the optical field are a subject of their own field of research named "singular optics" [38], and they provide a fascinating window into the fine structure of light. Caustics and dislocations come hand in hand, but also deformation of amplitude surfaces can dramatically change the dynamics of vortex lines [39]. A similar effect found in our system will be described in more detail in 4.

Phase singularities or dislocations, as otherwise called due to analogy with dislocations in crystalline materials, are lines of undefined phase in 3D optical fields with zero intensity [40, 41]. Later, the term "optical vortex" was introduced, drawing inspiration from fluid vortices, since the light twists around the dislocation line like a screw [42, 43]. This fact is supported by the analysis of energy flow and the Poynting vector around the vortex line [44, 45]. Various techniques are used to generate optical vortices, from using special filters and holograms to directly encoding a specific phase pattern with dislocations into the laser beam. Applications of such beams with structured light cover a wide range of avenues, from trapping small particles to optical communications, quantum cryptography, imaging, spectroscopy, metrology, and more [38, 46–49]. A noteworthy example is optical tweezers [50], the invention of the 2018 Nobel Prize winner Ashkin, which is used to capture small, microscopic objects without direct contact. Although the original design involves a highly focused beam without a vortex, modifying the technique with vortex beams allows for additional benefits, such as reduced heat transfer, induced spin and orbital angular momentum for more precise particle manipulation, advanced trapping geometries, etc. [51, 52].

Optical vortices, similar to vortices in fluids, can self-organize into intricate shapes, such as helices, braids, rings and knots [53]. Knots, being the most complex structure, appear spontaneously and are unstable under perturbation [54–56]. Nevertheless, vortex knots have fascinated scientists for centuries, notably giving rise to the theory of atoms being knotted vortices in aether by Kelvin [57]. The underlying formation mechanism of vortex knots in optics, fluids, or any turbulent media is currently unknown.

In contrast, vortex rings are straightforward. The original term "vortex ring" is credited to Helmholtz and his study of smoke rings [58]. Vortex rings are natural to turbulent motion: in volcanic eruptions, ocean currents, intracardiac blood flow, acoustics, super-

fluids, Bose-Einstein condensates and hydromagnetics [59, 60]. In optics, arguably the first appearance of vortex rings is associated with Airy rings, dark rings that form near the focal plane on a circular aperture [61]. Rings, the unknots, are a precursor to knots in non-paraxial and multiple superimposed paraxial beams [53, 62]. Understanding how rings form in a controlled environment may yield valuable information on how knots form. Interference of two co-propagating Gaussian beams can produce a vortex ring under controlled conditions by varying the diameters and amplitudes of beams [63]. Expanding on that concept and replacing one beam with a plane wave not only drastically simplifies the system but also allows for generating multiple rings and observing topological reactions [64].

Topological reactions (also topological events and topological transformations) are events that change the global topology of the field, for example, knotting and unknotting of a vortex line [53, 62]. In our case, such reactions change the number of rings. Basic reactions can be categorized into two: the elliptic (birth and death of a ring) and the hyperbolic (reconnection) [65]. There is also a pairwise creation or annihilation of counter-rotating singularities [66], which requires a strict radial symmetry [64]. Breaking the radial symmetry decomposes such reaction into the two aforementioned basic types [67]. Furthermore, the topological events mapped onto the control parameters domain can be arranged into one of the seven elementary catastrophes [68–70].

This thesis addresses several key topics and problems that exist in the aforementioned context using our model: the elliptic Gaussian beam and the co-propagating plane wave in superposition. Firstly, an exhaustive derivation of the elliptic Gaussian beams is provided, with a discussion on the quadrupole symmetry and its effects on the beam envelope. Secondly, a detailed overview of topological reactions in the system is presented, from the most basic single-ring nucleation to complex multiple-ring reconnections. Thirdly, I introduce catastrophes that appear in our system as the control parameters are varied, specifically cusp and butterfly, how they impact the topological events and their connection to the caustic surfaces of the beam.

In a broader context, this thesis aims to provide insights that can deepen our understanding of the fine structure of light in a system that can be replicated using accessible lab equipment. This in turn may be useful in the advancement of the theoretical foundation of optics and the development of various photonic technologies. Likewise, this work may share some valuable information to pinpoint specifics of the mechanisms that cause spontaneous knotting of vortex lines in non-linear systems.

2 MODEL AND BACKGROUND

This section provides the essential mathematical and physical context relevant to the subject of the thesis. The first part begins with a derivation of the paraxial wave equation and, subsequently, the Gaussian laser beam envelope. This is followed by a discussion of optical vortices and topological transformations. Expanding on these two topics, the next part contains a summary on vortex rings in radially symmetric Gaussian beams, based on the previous work of my supervisor Prof. Desyatnikov [64]. Finally, the last part offers a brief background on catastrophe theory.

2.1 Paraxial laser beams

Starting with Maxwell's equations in free space:

$$\nabla \cdot \mathbf{E} = 0 \tag{2.1a}$$

$$\nabla \times \mathbf{E} = -\frac{\partial \mathbf{B}}{\partial t} \tag{2.1b}$$

$$\nabla \cdot \mathbf{B} = 0 \tag{2.1c}$$

$$\nabla \times \mathbf{B} = \frac{1}{c^2}\frac{\partial \mathbf{E}}{\partial t} \tag{2.1d}$$

A double curl of a vector field $\mathbf{F}$ can be expanded into $\nabla \times \nabla \times \mathbf{F} = \nabla(\nabla \cdot \mathbf{F}) - \nabla^2 \mathbf{F}$. This approach applied to (2.1b) and (2.1d) leaves only the vector Laplacian part, since the term $\nabla \cdot \mathbf{F}$ cancels out for both $\mathbf{E}$ and $\mathbf{B}$ as a consequence of (2.1a) and (2.1c). Another simplification rule $\nabla \times \left(\frac{\partial \mathbf{F}}{\partial t}\right) = \frac{\partial}{\partial t}(\nabla \times \mathbf{F})$ can be applied to the right-hand sides of (2.1b) and (2.1d), and by substituting the result, the wave equations are obtained:

$$\nabla^2 \mathbf{E} - \frac{1}{c^2}\frac{\partial^2 \mathbf{E}}{\partial t^2} = 0 \qquad\qquad \nabla^2 \mathbf{B} - \frac{1}{c^2}\frac{\partial^2 \mathbf{B}}{\partial t^2} = 0 \tag{2.2}$$

A desired solution to (2.2) is a monochromatic beam with a frequency ω. It is important to note that these types of beams are an idealization - even the most perfect laser still emits light in a narrow band of frequencies. Nevertheless, a monochromatic approximation is still in good agreement with physical observations.

The electric and magnetic fields of the beam with a spatial vector component $\boldsymbol{\mathcal{E}}(\mathbf{r})$ and $\boldsymbol{\mathcal{B}}(\mathbf{r})$ are:

$$\mathbf{E}(\mathbf{r}, t) = \boldsymbol{\mathcal{E}}(\mathbf{r}) \exp(-i\omega t) \qquad\qquad \mathbf{B}(\mathbf{r}, t) = \boldsymbol{\mathcal{B}}(\mathbf{r}) \exp(-i\omega t) \tag{2.3}$$

Plugging (2.3) into the wave equation (2.2) will produce the Helmholtz equation, which is the eigenvalue problem of the vector Laplacian where $k = \omega/c$ is the wavenumber:

$$\nabla^2 \boldsymbol{\mathcal{E}} - k^2 \boldsymbol{\mathcal{E}} = 0 \qquad\qquad \nabla^2 \boldsymbol{\mathcal{B}} - k^2 \boldsymbol{\mathcal{B}} = 0 \tag{2.4}$$

From now on I only consider the electric field, as the magnetic field can be easily deduced from it. In addition to the monochromatic approximation, I also introduce the paraxial approximation $\left|\frac{\partial^2 E}{\partial z^2}\right| \ll k\left|\frac{\partial E}{\partial z}\right|$, where $E(\mathbf{r}, z)$ is the scalar amplitude distribution, assuming that the vector component containing k can be expressed separately s.t. $\boldsymbol{\mathcal{E}}(\mathbf{r}, z) = E(\mathbf{r}, z)\exp(ikz)$. The vector term only contains z to satisfy the paraxial approximation, since the dominant wave vector must be in the z-direction. Finally, substituting $\boldsymbol{\mathcal{E}}(\mathbf{r})$ into (2.4), the Helmholtz equation in the paraxial regime is obtained:

$$2ik\frac{\partial E}{\partial z} + \frac{\partial^2 E}{\partial x^2} + \frac{\partial^2 E}{\partial y^2} = 0, \tag{2.5}$$

The paraxial equation has many solutions, but the one I am specifically interested in describes the beam with the Gaussian amplitude distribution. This provides two conditions for the ansatz: the transverse profile must be of the Gaussian function, and as $z \to \pm\infty, E \to 0$. The obvious choice is $\frac{1}{a(z)}\exp\left(-\frac{r^2}{a(z)}\right)$; plugging the ansatz into (2.5) yields the following simple differential equation:

$$a'(z) = \frac{2i}{k} \tag{2.6}$$

The solution is the family of linear functions $a(z) = \frac{2i}{k}z + C$. To solve for C, a parameter called the beam waist w_0 is defined s.t. $a(0) = w_0^2$, which controls the beam width at the cross-section on the focal plane. With the condition $E(0, 0) = E_0$, the resulting equation describing the complex amplitude of the Gaussian beam is then:

$$E(r, z) = \frac{E_0}{1 + iz/z_R}\exp\left(-\frac{r^2}{w_0^2(1 + iz/z_R)}\right) \tag{2.7}$$

Here, $z_R = \frac{kw_0^2}{2}$ is called the Rayleigh range, the distance from the waist at which the beam's transverse section doubles in area. In some literature, it is also called the diffraction length since it determines how fast or slow the beam starts diverging, given the waist size w_0. The smaller w_0, the faster the beam diffracts, and vice versa. Fig. 1 depicts the intensity profile of the Gaussian beam with parameters w_0 and z_R.

Of course, interpreting a complex equation in real physical terms is not easy; separating the absolute value part, which describes the amplitude, and the argument part, which stands for the phase, makes it more intuitive:

$$E(r, z) = \frac{E_0}{\sqrt{1 + z^2/z_R^2}}\exp\left(-\frac{r^2}{w_0^2(1 + z^2/z_R^2)} + i\frac{r^2 z/z_R}{w_0^2(1 + z^2/z_R^2)} - i\tan^{-1}\frac{z}{z_R}\right) \tag{2.8}$$

Note the arctangent term, which is often referred to as the Gouy phase. The term is responsible for the phase anomaly where a beam acquires an additional $+\pi$ radians of phase as it propagates through the focal plane.

To further simplify the notation, two functions are introduced: the beam envelope

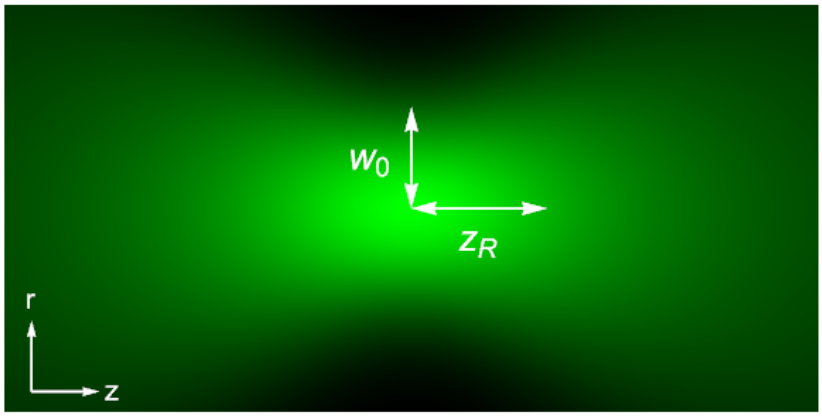

Figure 1: Intensity profile $|E|^2$ of the Gaussian beam along the optical axis z.

radius $w(z) = w_0\sqrt{1 + z^2/z_R^2}$ and the wavefront curvature radius $R(z) = z(1 + z_R^2/z^2)$. The final equation governing the electric field of the Gaussian beam is thus:

$$E(r, z) = E_0 \frac{w_0}{w(z)} \exp\left(-\frac{r^2}{w^2(z)} + i\frac{r^2 z_R}{w_0^2 R(z)} - i\tan^{-1}\frac{z}{z_R}\right) \tag{2.9}$$

The beam governed by (2.8) is the so-called fundamental mode, using which higher-order modes of the Gaussian beam can be constructed. The Hermite Gaussian (E_{nl}^{HG}) and the Laguerre Gaussian (E_{mp}^{LG}) modes are notable examples, one arising from the rectangular symmetry and the other from the radial symmetry. As the names suggest, the transverse profile of such beams is governed by the Hermite and Laguerre polynomials.

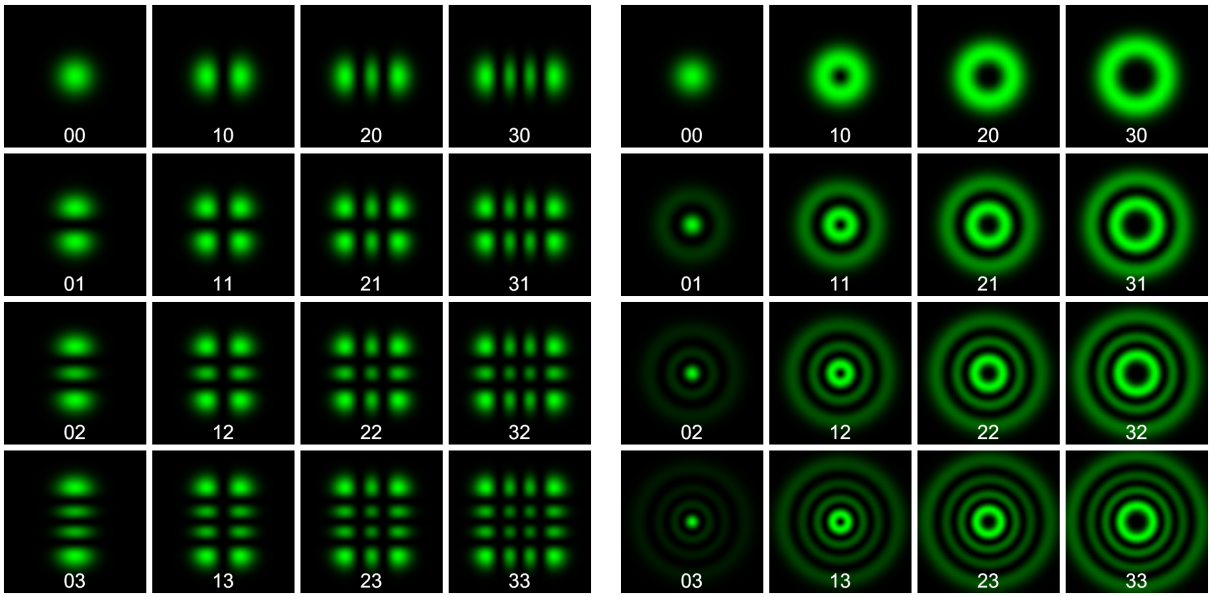

Figure 2: Intensity profiles ($|E|^2$) of Hermite-Gaussian (left) and Laguerre-Gaussian (right) modes at the focal plane $z = 0$. The numbers on the bottom represent n, l and m, p indices in E_{nl}^{HG} and E_{mp}^{LG}.

$$E_{nl}^{HG}(x,y,z) = E_0 \frac{w_0}{w(z)} H_n\left(\frac{x\sqrt{2}}{w(z)}\right) H_l\left(\frac{y\sqrt{2}}{w(z)}\right) \exp\left(-\frac{x^2}{w^2(z)}\right) \exp\left(-\frac{y^2}{w^2(z)}\right) \times \\ \times \exp\left(i\frac{(x^2+y^2)z_R}{w_0^2 R(z)} - i(1+n+l)\tan^{-1}\frac{z}{z_R}\right) \tag{2.10a}$$

$$E_{mp}^{LG}(r,\theta,z) = E_0 \frac{w_0}{w(z)} \left(\frac{r\sqrt{2}}{w(z)}\right)^{|m|} L_p^{|m|}\left(\frac{2r^2}{w^2(z)}\right) \exp\left(-\frac{r^2}{w^2(z)}\right) \times \\ \times \exp\left(i\frac{r^2 z_R}{w_0^2 R(z)} + im\theta - i(1+|m|+2p)\tan^{-1}\frac{z}{z_R}\right) \tag{2.10b}$$

Fig. 2 presents the intensity profiles of some E_{nl}^{HG} and E_{mp}^{LG} modes, generated numerically. HG and LG modes can also be combined to create even more complex beam profiles, such as the Ince Gaussian [71], Boyer-Wolf Gaussian [72], and Hypergeometric Gaussian modes [73], but those are beyond the scope of this thesis.

Instead, the attention is redirected to the E_{10}^{LG} mode to introduce optical vortices.

2.2 Optical vortices and topological events

Optical vortices are lines of undefined phase in 3D light fields. To initiate a discussion, first let us consider the simplest case: a beam with a vortex at the center. This model applies to the previously mentioned LG beams. Analyzing the phase profile of modes with nonzero azimuthal index m, which are also called the "doughnut" modes, reveals a phase singularity at the center of the transverse plane, as presented in Fig. 3. The vortex propagates along the optical axis z, creating a helical wavefront, with the phase rotating around the singularity point.

The field near the core of the vortex can be approximated as $E \simeq r^{|m|}\exp(im\theta)$ in cylindrical coordinates and $E \simeq (x + \mathrm{sign}(m)iy)^{|m|}$ in Cartesian coordinates. These approximations are similar to (2.10b) if $z = 0$ and terms containing r^2 are discarded. In this context, the index m is also called the winding number or the topological charge, which controls the number of windings by 2π around the singularity point.

The complex scalar field can be divided into two parts: the amplitude $|E|$ and phase $\arg E$; the latter is also often denoted as ψ s.t. the complex field is $E = |E|\exp(i\psi)$. The charge m is thus calculated as:

$$m = \frac{1}{2\pi}\oint_C \nabla\psi \cdot d\vec{l} \tag{2.11}$$

Here, C is a closed contour containing the singularity and $d\vec{l}$ is the vector length element.

The vortex appears at the intersection of planes described by $\mathrm{Re}\,E = 0$ and $\mathrm{Im}\,E = 0$. Considering the near field in Cartesian coordinates $E \simeq (x + \mathrm{sign}(m)iy)^{|m|}$, the real and imaginary terms are orthogonal to each other and thus cross strictly perpendicularly, creating the canonical vortex. As the name suggests, the canonical vortex is a perfectly symmetrical vortex, with the phase winding around the core linearly with respect to the

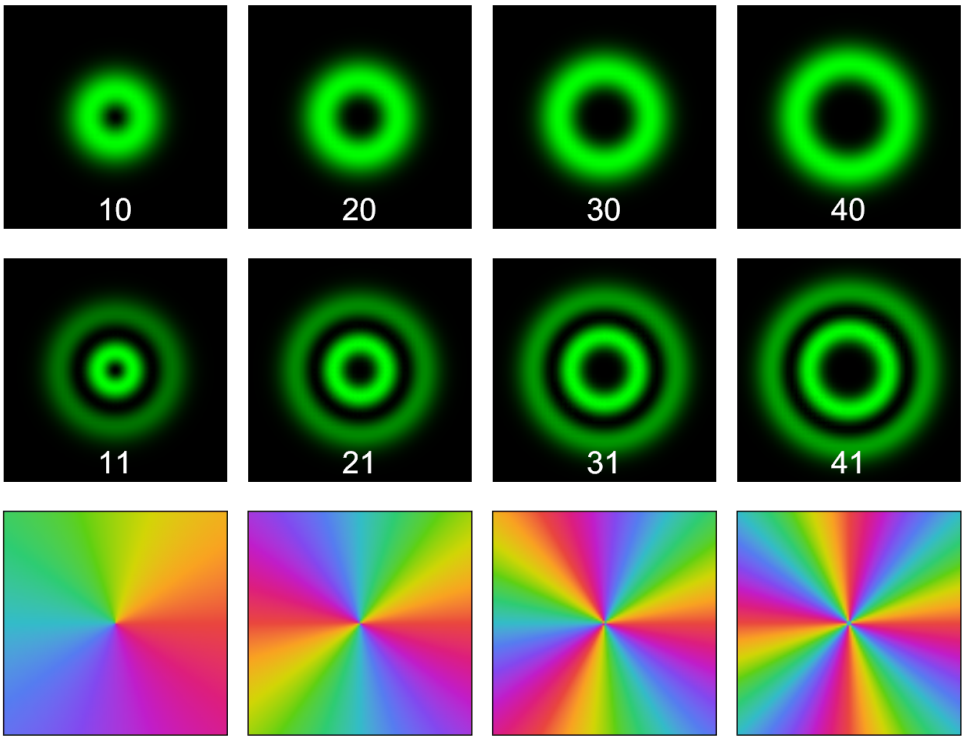

Figure 3: The intensity profiles of Laguerre-Gaussian "doughnut" modes and the corresponding phase profiles (bottom row).

angle θ. Canonical vortices with $|m| > 1$ split into other canonical vortices with unit charge under perturbations, either $m = -1$ or $m = +1$. The sign of m denotes the direction of rotation: positive if counter-clockwise and negative if clockwise.

One may say that the existence of canonical vortices also implies the existence of noncanonical vortices. Indeed, there is a whole class of vortices that diverge from the strict symmetric appearance, which earns them their name. They still carry the same integer-valued topological charge as the canonical counterparts, however, the winding of the phase is not linearly proportional to θ. Moreover, noncanonical vortices can be constructed by continuously deforming multiple canonical vortices with different m.

The field near the core of the noncanonical vortex can be approximated as $E \simeq a_x x + a_y y$, where a_x and a_y are complex parameters. Assuming that $a_x \neq 0$, the expression can be simplified to $E \simeq a_x(x + iAy)$. Here, $A = ia_y/a_x$ is called the noncanonical parameter, which controls the morphology of the vortex. For $A = \pm 1$, the near field simplifies to $E \simeq x \pm iy$, which is the canonical vortex with charge $m = \pm 1$. The sign of the real part of A determines the sign of m, but in real-life experimental scenarios, the topological charge of the noncanonical vortex can only be determined by interferometric means. To do so, it is necessary to get as close to the vortex and measure several distances associated with different intensity contour levels, such as the width, length of semi-major or semi-minor axes, average distance from center, etc. The iso-intensity contours around a noncanonical vortex often resemble a tilted ellipse instead of a perfect circle, which is why measurements of several contours are taken to accurately calculate A.

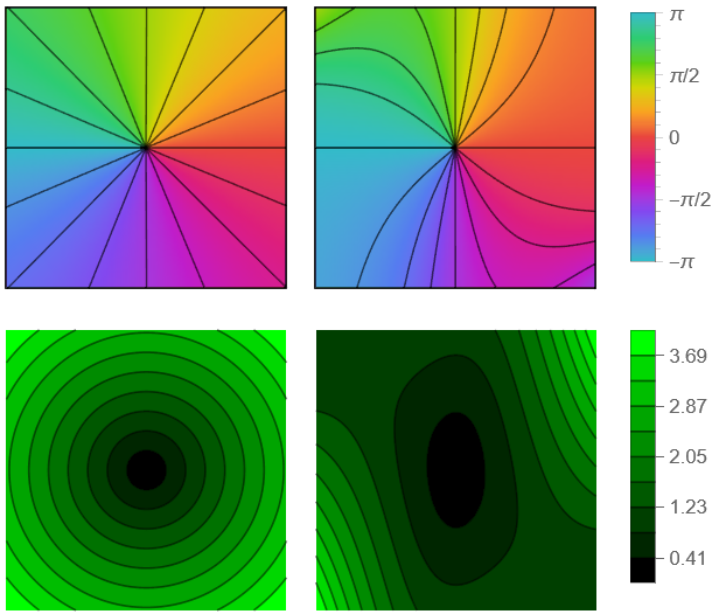

Figure 4: Iso-phase (top) and iso-amplitude contours (bottom) of a canonical vortex on the left and a noncanonical vortex on the right.

Noncanonical vortices are the most general types of isolated vortices stable under perturbations, and they naturally appear in a variety of turbulent media, such as speckle fields, for example. In our system, vortices appear to be noncanonical due to their asymmetric appearance even in the radially symmetric beams, which will be presented in more detail in the next section.

One last important topic for discussion is the topological reactions of optical vortex lines, also referred to as topological events or topological transformations. The two basic types of events categorized by Berry and Dennis [65] are a nucleation of a vortex ring from a point, called the "elliptic" event, and reconnection of two or more vortex lines touching on a point, the "hyperbolic" event. Higher-order topological reactions can be created by combining these two.

The 3D field can be expressed as a combination of functions of real and imaginary parts: $E = \xi(\boldsymbol{\rho}, t) + i\eta(\boldsymbol{\rho}, t)$. Here, $\boldsymbol{\rho} = (\boldsymbol{r}, z)$ with $\boldsymbol{r} = (x, y)$ and t is a real parameter of time. The field near the vortex can be approximated as $E \simeq t + iaz + \frac{1}{2}\boldsymbol{\rho} \cdot B \cdot \boldsymbol{\rho}$, where a is a real arbitrary constant and B is a complex symmetric 3×3 matrix that determines the geometry of the field. An important term associated with the phase of a field is the vorticity $\boldsymbol{\Omega}$, a pseudovector of local spinning motion, defined as:

$$\boldsymbol{\Omega} = \nabla\xi \times \nabla\eta \tag{2.12}$$

When $\boldsymbol{\Omega} = 0$, which happens if $\nabla\xi$ and $\nabla\eta$ are parallel or anti-parallel to each other, the field has no spinning potential, i.e. no vortex motion can be observed. Thus, at points where $\boldsymbol{\Omega} = 0$ line intersects with the vortex, the topology of the vortex line changes,

inciting a reaction. Using that information, and since the vortex lines lie on $\xi = \eta = 0$, $t + iaz + \frac{1}{2}\boldsymbol{\rho} \cdot B \cdot \boldsymbol{\rho} = 0$ can be separated into the real and imaginary parts:

$$t + \frac{1}{2}\boldsymbol{r} \cdot \operatorname{Re} B_\perp \cdot \boldsymbol{r} + z \operatorname{Re} \boldsymbol{b} \cdot r + \frac{1}{2} z^2 \operatorname{Re} B_{33} = 0 \tag{2.13a}$$

$$az + \frac{1}{2}\boldsymbol{r} \cdot \operatorname{Im} B_\perp \cdot \boldsymbol{r} + z \operatorname{Im} \boldsymbol{b} \cdot r + \frac{1}{2} z^2 \operatorname{Im} B_{33} = 0 \tag{2.13b}$$

Here, $B_\perp = \left(\begin{smallmatrix} B_{11} & B_{12} \\ B_{12} & B_{22} \end{smallmatrix}\right)$ and $\boldsymbol{b} = \left(\begin{smallmatrix} B_{13} & B_{23} \end{smallmatrix}\right)$. The geometry of the vortex mainly depends on the surface described by (2.13a). An important term that determines the curvature of the surface is $\operatorname{Re} B_\perp$. At $t = 0$, $\det \operatorname{Re} B_\perp > 0$ represents an ellipse shrinking to a point, which is the elliptic event, and $\det \operatorname{Re} B_\perp < 0$ represents two hyperbolas reconnecting on a point, hence the hyperbolic event.

With the essential information on optical vortices and topological reactions covered, I can now transition into the discussion on vortex rings.

2.3 Vortex rings in radially symmetric Gaussian beams

First, dimensionless coordinates (x, y, t) are introduced, where the radial coordinates (x, y) are scaled by w_0, $t = z/z_R$ is the characteristic "time", and $E_0 = 1$.

In this system of dimensionless coordinates, the fundamental paraxial equation (2.5) is transformed into:

$$4i\frac{\partial E}{\partial t} + \frac{\partial^2 E}{\partial x^2} + \frac{\partial^2 E}{\partial y^2} = 0, \tag{2.14}$$

and the fundamental Gaussian mode (2.7) can be reformulated as:

$$E(r,t) = \frac{1}{1+it} \exp\left(-\frac{r^2}{1+it}\right) \tag{2.15}$$

$$= \frac{1}{\sqrt{1+t^2}} \exp\left(-\frac{r^2}{1+t^2} + i\frac{r^2 t}{1+t^2} - i\tan^{-1} t\right) \tag{2.16}$$

The superposition of the Gaussian beam with phase α and a co-propagating plane wave with the relative amplitude P and phase β is then:

$$\mathcal{E} = E(r,t)\exp\left(i\kappa t + i\alpha\right) + P\exp\left(i\kappa t + i\beta\right) \tag{2.17}$$

Here, $\kappa = kz_R$ is the dimensionless wavenumber. In a similar manner, superposition of a beam and tilted plane wave can be constructed; the results are presented in appendix III. The goal is to find the zeros of (2.17), which is obtained by solving for the following simplified equation:

$$E(r,t) = P\exp(i\phi) \tag{2.18}$$

The relative phase parameter ϕ is defined as $\phi = \pi + \beta - \alpha$. The solution to (2.18) lies

on the intersection of the absolute value and the argument:

$$|E(r,t)| = \frac{1}{\sqrt{1+t^2}} \exp\left(-\frac{r^2}{1+t^2}\right) = P \tag{2.19a}$$

$$\psi(r,t) = \frac{r^2 t}{1+t^2} - \tan^{-1} t = \phi + 2\pi n \tag{2.19b}$$

The first equation (2.19a) describes amplitude iso-surfaces in the form of spheroids. There are two distinct shapes a spheroid can take, depicted in Fig. 5: a simple ellipsoid for $P > 1/\sqrt{e} \approx 0.61$ (green), and a "dumbbell" with two maxima at $t = \pm\sqrt{1/(P^2 e) - 1}$ and a minima at $t = 0$ for $P < 1/\sqrt{e}$ (cyan).

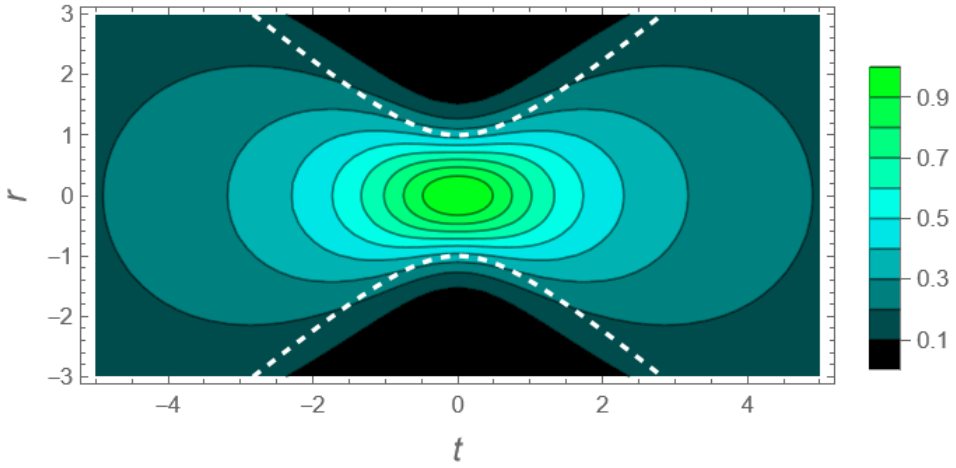

Figure 5: Contours of amplitude iso-surfaces $|E| = P$ of a radially symmetric Gaussian beam and the beam radius $w(t) = \sqrt{1+t^2}$ (white dashed line).

Maxima of the spheroids are always contained inside the hyperboloid of beam radius $w(t)$, and the iso-surfaces cross the hyperboloid at $(r_i, t_i) = (1/Pe, \pm\sqrt{(Pe)^{-2} - 1})$. The intersection point will play an important role later when it comes to topological reactions.

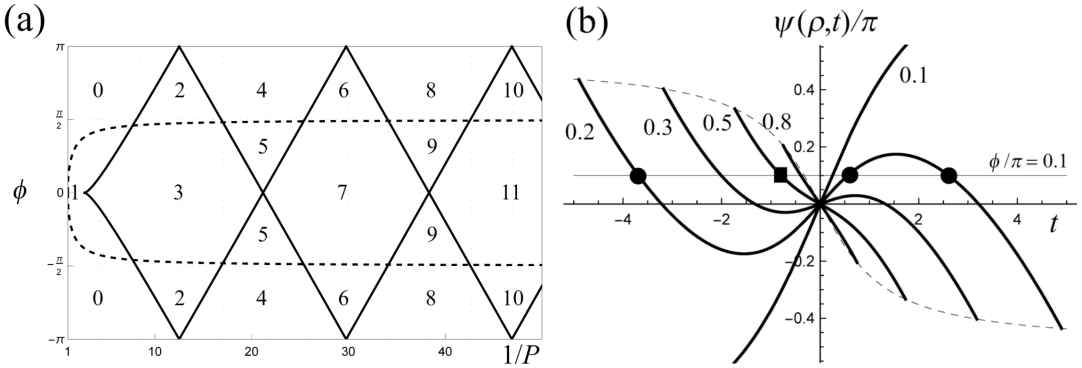

Figure 6: (a) Number of vortex rings in (P, ϕ) parameter domain and (b) the phase $\psi(\rho(t), t)$ plotted for $P = 0.1, 0.2, 0.3, 0.5$, and 0.8. The dashed line corresponds to the axial extent of spheroids $\tan^{-1} t$; the thin horizontal line $\phi = \pi/10$ determines the location of vortex rings in Fig. 7: square in 7(a) and dots in 7(b). Figures from [64].

In (2.19a), the equation can be rearranged as $r^2 = \rho(t)^2 = -(1+t^2)\ln\left(P\sqrt{1+t^2}\right)$,

then used to express the equation of phase at spheroids:

$$\psi(\rho(t), t) = -t \ln\left(P\sqrt{1+t^2}\right) - \tan^{-1} t = \phi + 2\pi n \tag{2.20}$$

In this setup, two types of topological reactions are identified, one happening on the optical axis $r = 0$ and the other at the points of intersection (r_i, t_i). The first one, marked as the dashed line in Fig. 6(a), is the birth or death of a single ring, which occurs at the endpoints of the spheroid $t = \pm\sqrt{P^{-2} - 1}$ for $\phi = \pm\cos^{-1} P$. This type of topological event changes the number of rings in the system by 1, meaning that no pairs are created simultaneously on the optical axis. The ring nucleates from a single point on one side of the spheroid and annihilates on the other. The birth/death of a ring also appears to be a stable event, unchanged when the radial symmetry is broken, which is not possible for the second type of reaction.

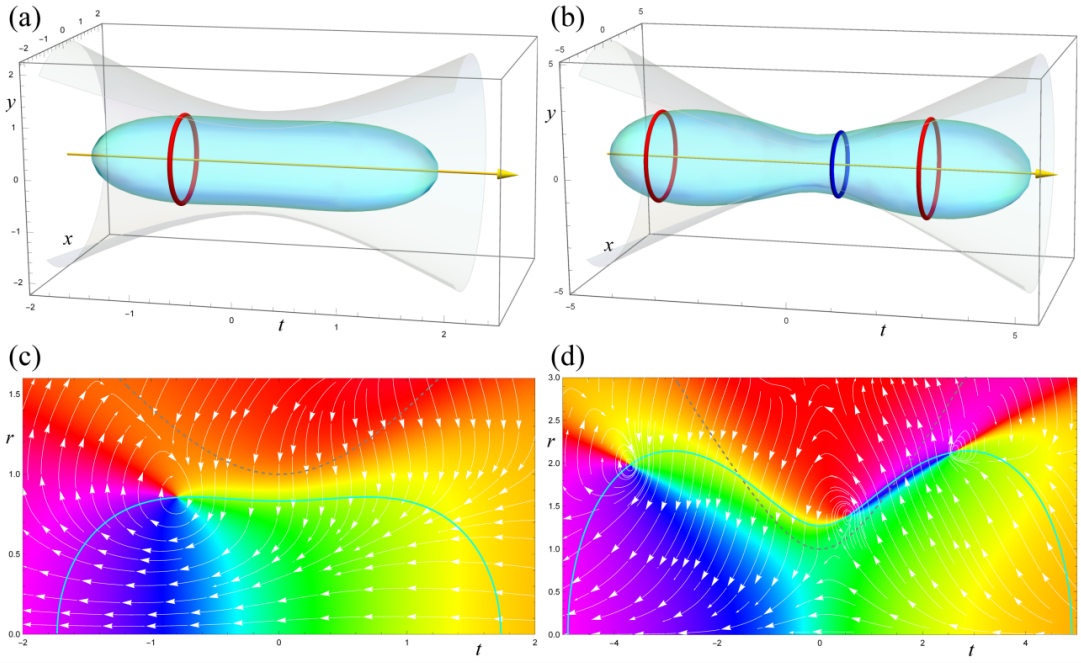

Figure 7: (a,b) Vortex rings on spheroids and (c,d) corresponding phase (hue colormap) and current (white arrows) for the relative amplitudes $P = 0.5$ in (a,c) and $P = 0.2$ in (b,d). Gray surfaces in (a,b) and dashed lines in (c,d) show the beam radius $r = \sqrt{1+t^2}$. In both cases, $\phi = \pi/10$. Figures from [64].

The second event, which happens at the intersection plane of the spheroids and the hyperboloid of beam radius, is the mutual creation and annihilation of a counter-propagating pair of rings. The location of the intersection plane along the optical axis t_i also coincides with the extrema of $\psi(\rho, t)$, which are presented in Fig. 6(b). The exact location of such extremas, and consequently, events, is $t = \pm\sqrt{(Pe)^{-2} - 1}$ at $\phi = \pm(\sqrt{(Pe)^{-2} - 1} - \tan^{-1}\sqrt{(Pe)^{-2} - 1})$. In the parameter space displayed in Fig. 6(a), the reaction is marked with the solid black line, changing the number of rings by 2, as expected.

Unlike the previously mentioned reaction, this one is a product of strict radial symmetry. When the symmetry is broken, as in elliptic beams, the reaction decomposes into a combination of pairwise nucleation and reconnection.

Paying attention to the hue colormaps in Fig. 7(c,d), the phase around the vortices is not distributed symmetrically, which is especially noticeable in Fig. 7(d). This means that the vortices are noncanonical, with the topological charge $m = \pm 1$. In fact, the charge is determined by $m = \text{sign}(\rho^2 - t^2 - 1)$, which is negative if the ring is inside the hyperboloid $r = \sqrt{1 + t^2}$ and positive if outside.

As mentioned already, this system follows a round symmetry, which generates perfectly circular rings. In elliptic beams, however, this is no longer possible since breaking the symmetry introduces perturbations that change the topology of vortex lines. But before introducing elliptic beams and associated topological reactions, I must present another short review of a crucial topic - catastrophe theory.

2.4 The cusp and the butterfly catastrophes

In experiments, the reproducibility of the exact conditions is not realistic. One or multiple other parameters, such as the temperature or concentration of a solution, will always differ slightly from the ideal. In general, it is expected that tiny differences will not affect the outcome greatly - such property is called structural stability. However, that is not always the case; sometimes, slight perturbations do cause dramatic changes. Moreover, sudden shifts in state can actually be traced in the parameter domain of said system, at which point the catastrophe theory enters the picture.

In mathematical terms, varying certain parameters can cause critical points of a potential function to appear or disappear. Usually, such "catastrophic" values of parameters can be identified by taking the first and subsequent higher-order derivatives of a potential function and equating them to zero. By mapping such points onto the relevant parameter space, specific patterns appear, which were categorized by Thom into the seven elementary catastrophes: fold, cusp, swallowtail, butterfly, hyperbolic umbilic, elliptic umbilic, and parabolic umbilic [17]. I will spare technical details irrelevant to the topic and focus only on the two types of elementary catastrophes present in our system: the cusp and the butterfly.

First is the cusp catastrophe, or Riemann-Hugoniot, as otherwise called. The general potential $V(x)$ with two arbitrary parameters u and v is in the following form:

$$V(x) = x^4 + ux^2 + vx \tag{2.21}$$

The surface of zeros of the first derivative $dV/dx = 0$ is called the equilibrium surface:

$$4x^3 + 2ux + v = 0, \tag{2.22}$$

and the set of solutions that satisfy $d^2V/dx^2 = 0$ is called the singularity set:

$$12x^2 + 2u = 0, \tag{2.23}$$

Here, x can be easily eliminated from (2.22) by solving (2.23), which results in $x = (-u/6)^{1/2}$. Plugging x into (2.22) yields the bifurcation set (u, v):

$$8u^3 + 27v^2 = 0 \tag{2.24}$$

Plotting (2.24) reveals a curve with a sharp pinched corner on $(u, v) = (0, 0)$ as presented in Fig. 8(a), which earns this catastrophe its name – the cusp. When $u > 0$, the potential only experiences smooth changes as v is varied; in particular, there is only one extremum point. However, at $u < 0$, the parameter domain is split into the three regions separated by the branches of the cusp in Fig. 8(a). Outside those branches, the potential function obtains inflection points, while inside, the function now has three pronounced extremums.

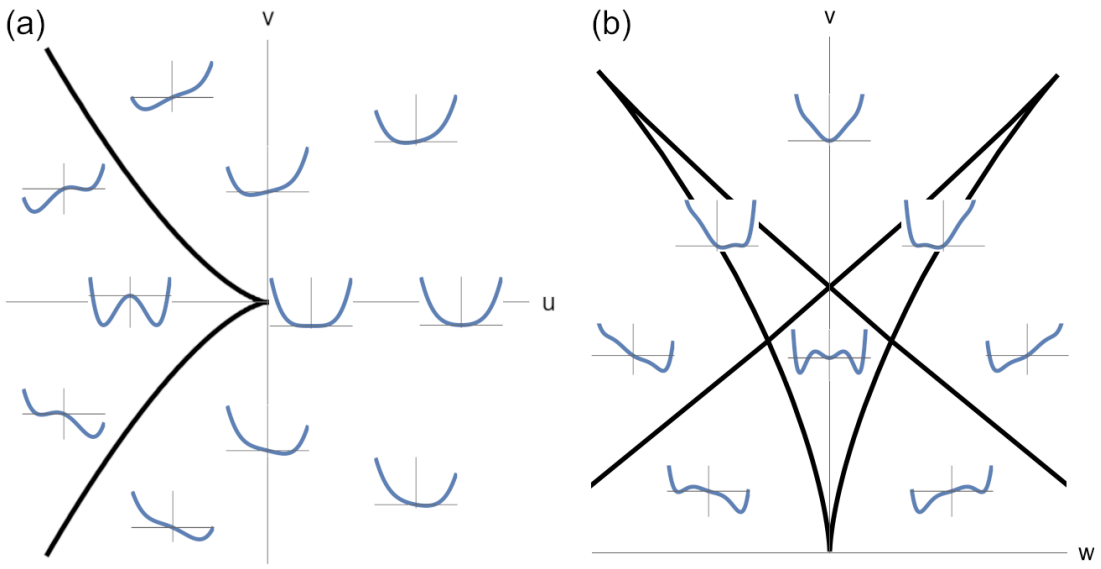

Figure 8: Bifurcation set of (a) the cusp catastrophe and (b) the butterfly catastrophe. The blue curves are the corresponding shapes of potential functions $V(x)$.

The butterfly catastrophe is a bit more complicated than the cusp. The potential here is:

$$V(x) = x^6 + tx^4 + ux^3 + vx^2 + wx, \tag{2.25}$$

which involves 4 parameters, so it will not be as easy to visualize. In fact, no single curve represents this catastrophe - there is a whole family of related curves that are referred to as the butterfly. The equilibrium surface of (2.25) is:

$$6x^5 + 4tx^3 + 3ux^2 + 2vx + w = 0, \tag{2.26}$$

and the singularity set:

$$30x^4 + 12tx^2 + 6ux + 2v = 0 \tag{2.27}$$

Rearranging the terms in the latter two equations enables expressing v and w in terms of x and parameters u, t:

$$v = -15x^4 - 6tx^2 - 3ux \tag{2.28a}$$

$$w = 24x^5 + 8tx^3 + 3ux^2 \tag{2.28b}$$

Now, if $t = u = 0$, then x can be eliminated, resulting in $(v/15)^5 = -(w/24)^4$, which is a simple cusp. But to see how the potential changes w.r.t. (u, t) parameters, the critical points of (2.28a) and (2.28b) need to be analyzed.

$$dv/dx = -60x^3 - 12tx - 3u \tag{2.29a}$$

$$dw/dx = 120x^4 + 24tx^2 + 6ux \tag{2.29b}$$

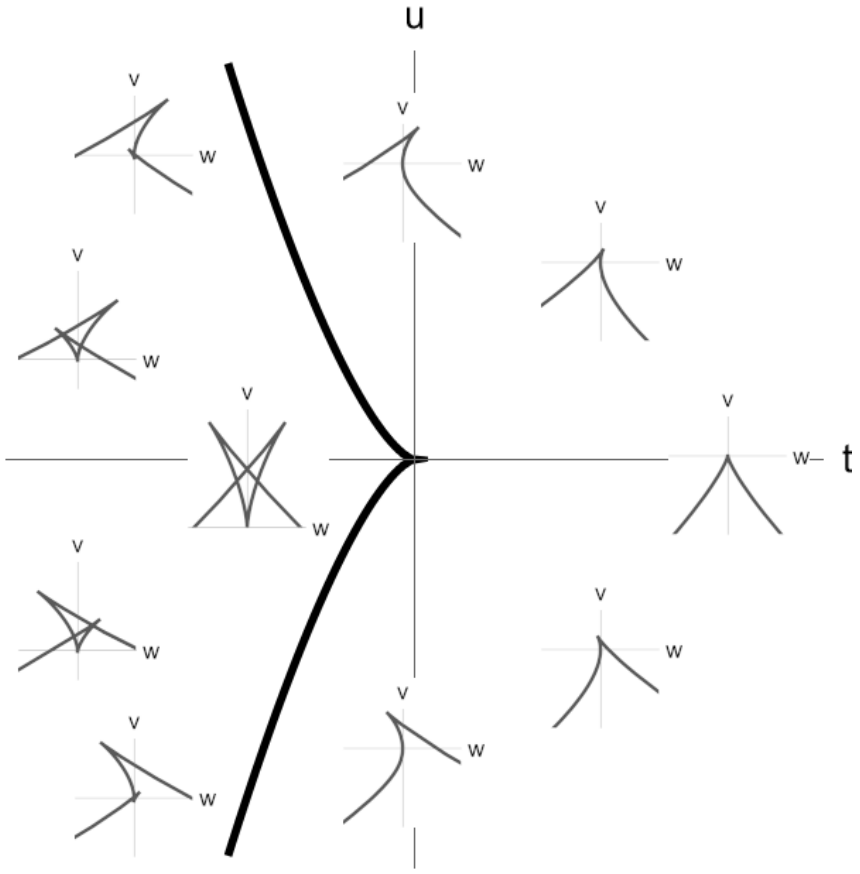

Figure 9: Bifurcation sets (gray) of the butterfly for different values of u and t.

Both derivatives vanish if the common factor $20x^3 + 4tx + u$ is also zero. The factor is a cubic equation, meaning that it can have either one or three real roots; the condition $(u/2)^2 < -(4t/3)^3$ determines that. If $t > 0$, u will appear complex, resulting in one real root, so a simple single cusped curve appears. However, at $t < 0$, three cusps appear,

merging into the signature butterfly shape, as presented in Figs. 8(b) and 9.

In regions outside the branches of the butterfly, the potential function (2.25) has one pronounced extremum point, which can be seen in Fig. 8(b). Inside the branches, the potential obtains either one additional minimum and one inflection point or two additional minima.

In our system, the characteristic phase acts as a potential function. Since critical points of the phase are directly tied to the topological reactions, I will describe a new class of events that result from the catastrophes in section 4.

With the important context introduced, I can finally proceed to my work; the results are presented in the following sections.

3 TOPOLOGICAL REACTIONS OF VORTEX RINGS IN ELLIPTIC GAUSSIAN BEAMS

This section consists of three parts.

The first provides a detailed derivation of the equation governing the Gaussian beam with an elliptic transverse profile. I introduce the three types of beams, categorizing them by parameters that describe their shape. A more detailed discussion on beam symmetries, special planes and how they might affect the geometry of rings follows, concluding the part.

The second introduces a numerical method of calculating the zeros of superposition, which correspond to the coordinates of the rings. The asymmetry does not allow the equations to be handled analytically as in the radially symmetric beams; to address that, I introduce a semi-analytical method, which involves a parametrization of transverse coordinates by t. Finally, I present how rings are arranged in the three types of beams.

The last part delves into topological reactions. I introduce the two categories of topological events that occur in the system: on-axis and off-axis, and explain how the beam symmetries influence their dynamics.

An important note is that in this section, I only consider beams that deviate from radial symmetry only slightly. Inducing ellipticity beyond what is presented here results in catastrophes and new sets of reactions to appear. Such occurrences will be presented in more detail in the next section.

3.1 Elliptic Gaussian beams

The fundamental solution to the dimensionless paraxial equation (2.14) is:

$$E_0(x,t;w,t_0) = \frac{w}{\sqrt{w^2 + i(t-t_0)}} \exp\left(-\frac{x^2}{w^2 + i(t-t_0)}\right) \tag{3.1}$$

A product of two Gaussians with different waist radii w and location of foci t_0 for x- and y-directions allows for the construction of the 2D Gaussian with elliptic transverse profile:

$$E(x,y,t) = E_0(x,t;w_x,d/2)E_0(y,t;w_y,-d/2) \tag{3.2}$$

The parameter d here is the distance of the focal plane separation that causes astigmatism. To reduce the parameter domain, I introduce the "ellipticity" parameter $\epsilon \in (0,\pi/2)$ s.t. $w_x = \sqrt{2}\cos\epsilon$ and $w_y = \sqrt{2}\sin\epsilon$. If $\epsilon > \pi/4$, the waist is elongated along the y-axis, and along the x-axis if $\epsilon < \pi/4$.

Setting $\epsilon = \pi/4$ and $d = 0$ recovers the radially symmetric beam described in (2.15).

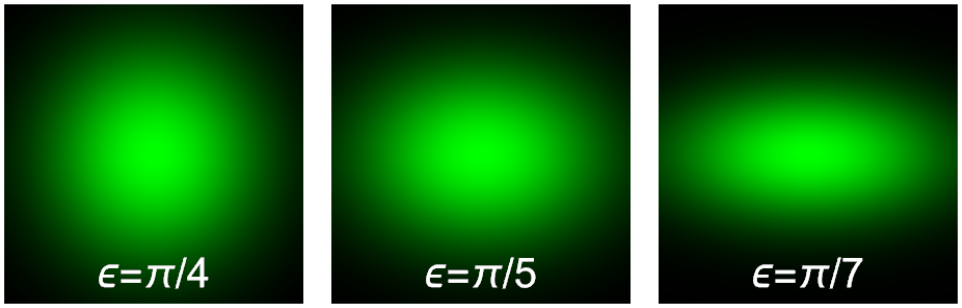

Figure 10: Intensity profiles of an elliptic beam $d = 0$ for various ϵ at the focal plane $t = 0$.

The full expression for the elliptic Gaussian beam is then:

$$E(x,y,t) = \frac{\sin 2\epsilon}{\sqrt{(2\cos^2\epsilon + i(t-d/2))(2\sin^2\epsilon + i(t+d/2))}} \times \tag{3.3}$$

$$\times \exp\left(-\frac{x^2}{2\cos^2\epsilon + i(t-d/2)} - \frac{y^2}{2\cos^2\epsilon + i(t-d/2)}\right) \tag{3.4}$$

Dividing into the amplitude and phase parts results in the following:

$$|E(x,y,t)| = \frac{\sin 2\epsilon}{\left((4\cos^4\epsilon + (t-d/2)^2)(4\sin^4\epsilon + (t+d/2)^2)\right)^{1/4}} \times \\ \times \exp\left[-\frac{2x^2\cos^2\epsilon}{4\cos^4\epsilon + (t-d/2)^2} - \frac{2y^2\sin^2\epsilon}{4\sin^4\epsilon + (t+d/2)^2}\right] \tag{3.5}$$

$$\arg E(x,y,t) = \frac{x^2(t-d/2)}{4\cos^4\epsilon + (t-d/2)^2} + \frac{y^2(t+d/2)}{4\sin^4\epsilon + (t+d/2)^2} - \\ - \frac{1}{2}\left(\arctan\frac{t-d/2}{2\cos\epsilon^2} + \arctan\frac{t+d/2}{2\sin\epsilon^2}\right) \tag{3.6}$$

A rotating elliptic Gaussian beam can be constructed using (3.3), but since it is out of the scope of this section, the derivation will be presented in appendix I.

All beams governed by (3.3) are elliptic, except for the radial case ($\epsilon = \pi/4, d = 0$). However, for convenience's sake, we distinguish three basic types of beams according to the parameters used to govern their shape as elliptic ($\epsilon \neq \pi/4, d = 0$), astigmatic ($\epsilon = \pi/4, d \neq 0$), and elliptic-astigmatic ($\epsilon \neq \pi/4, d \neq 0$).

The elliptic beam, depicted in Fig. 11 (a), has different waist radii in x- and y-directions with both foci located on the same transverse plane $t = 0$. Due to that, the transverse profile at the focal plane $t = 0$ is elliptic. But since the beam diffracts faster in the direction with smaller w, the profile of the beam changes as it propagates accordingly. The beam has two planes at $t_c = \pm\sin 2\epsilon$ where it appears circular, and the ellipticity inverts for $|t| > |t_c|$. The focal plane $t = 0$ acts as a plane of symmetry, meaning that the beam profile is invariant w.r.t. $t \to -t$.

The astigmatic beam has the same width w in both directions, but the foci are separated by the distance d. Despite having the same diffraction rates, the transverse profile

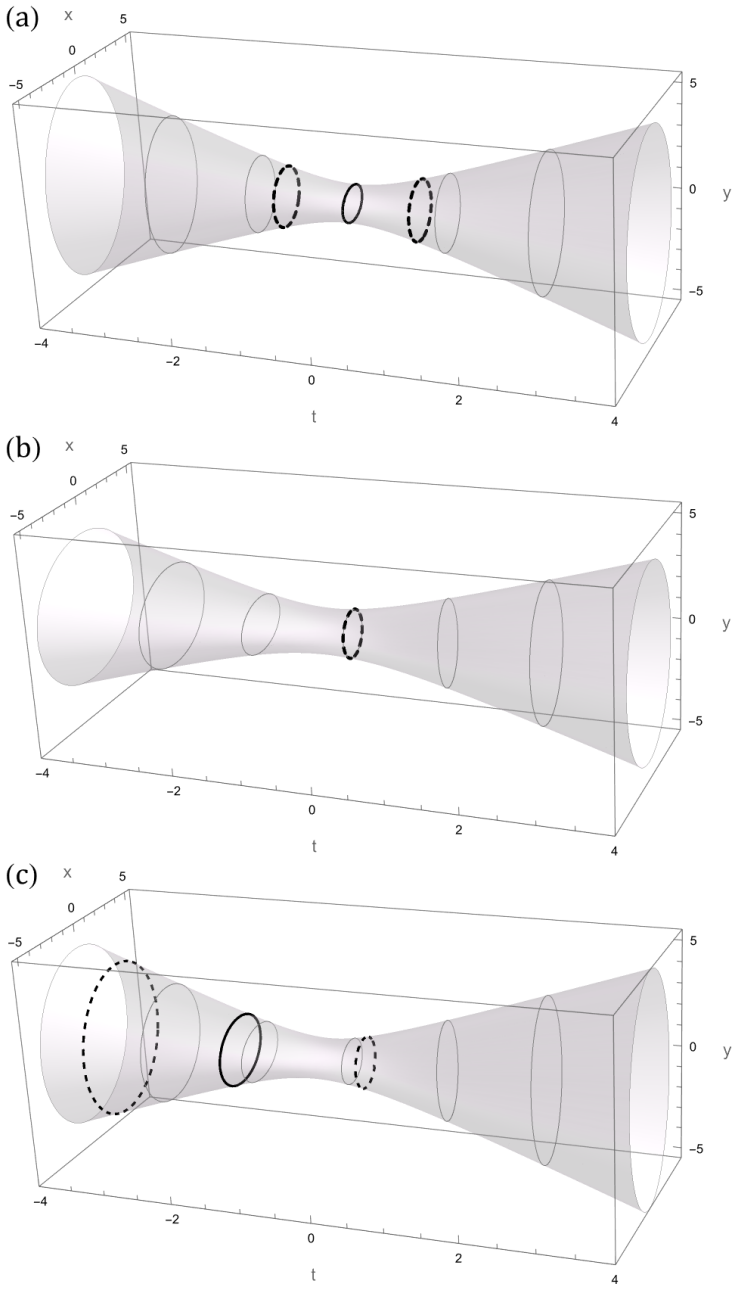

Figure 11: Beam-shapes of (a) elliptic beam with $(\epsilon, d) = (\pi/5, 0)$, (b) astigmatic beam $(\pi/4, 1)$, and (c) elliptic–astigmatic beam $(\pi/5, 1)$. Dashed lines show circular beam profiles at $t = t_c$, and solid black lines show the profiles at the planes $t = t_*$.

is still elliptic due to the separation of focal planes. The beam does not appear circular anywhere except for $t = 0$. Similar to the elliptic beam, the beam profile can be recovered if $t \to -t$, but in addition to that, the inversion must be accompanied by either $d \to -d$ or a rotation by $\pi/2$ radians.

The elliptic-astigmatic beam is the combination of the latter two, as the name suggests; the waist radii w are different, and the focal planes are separated by the distance d. The circular profiles appear at $t_c = t_* \pm \sin 2\epsilon \sqrt{1 + t_*^2}$ where $t_* = -d/(2 \cos 2\epsilon)$. Here, t_* is analogous to the symmetry plane $t = 0$ in elliptic beams and acts similarly when it comes

to the topological events, but the $t \to -t$ symmetry is broken.

The symmetries of the beam determine the configuration of vortex rings and affect the topological reactions, which are presented in the following subsection.

3.2 Vortex rings

The elliptic beams follow a quadrupole symmetry $(x, y) \to (\pm x, \pm y)$. Both (3.5) and (3.6) are elliptic in the transverse plane, so the intersection of the two can have zero roots, two roots on either $x = 0$ or $y = 0$ plane, or four roots on $(\pm x, \pm y)$, which is equivalent to finding intersection points of two concentric ellipses with different semi-major and semi-minor axes. Consequently, the rings appear deformed, unlike in the radial beams. The exception to that is the $t = t_*$ planes in elliptic and elliptic-astigmatic beams, where the rings can arrange flatly on the transverse plane.

To start the analysis, transverse coordinates (x, y) need to be expressed in polar coordinates $x = r\cos\varphi$ and $y = r\sin\varphi$. This will allow for the real and imaginary parts of (3.3) to be separated, which is a more efficient approach numerically than calculating the intersections of surfaces described by (3.5) and (3.6).

The beam envelope in the cylindrical coordinates (r, φ, t) is then:

$$\begin{aligned} E(r,\varphi,t) =& \frac{\sin 2\epsilon}{\sqrt{(2\cos^2\epsilon + i(t-d/2))(2\sin^2\epsilon + i(t+d/2))}} \times \\ & \times \exp\left(-\frac{r^2\cos^2\varphi}{2\cos^2\epsilon + i(t-d/2)} - \frac{r^2\sin^2\varphi}{2\sin^2\epsilon + i(t+d/2)}\right) \end{aligned} \tag{3.7}$$

Expanding all terms results in:

$$\begin{aligned} E(r,\varphi,t) =& \frac{\sin 2\epsilon}{\sqrt{(1+it)^2 + (d/2 + i\cos 2\epsilon)^2}} \times \\ & \times \exp\left(-\frac{r^2(1 + it + i\cos 2\varphi(d/2 + i\cos 2\epsilon))}{(1+it)^2 + (d/2 + i\cos 2\epsilon)^2}\right) \end{aligned} \tag{3.8}$$

Unlike in the radial case, rings in this setup cannot be found analytically; the equations cannot be simplified to a more compact form to allow that. Instead, I use a semi-analytical method to obtain the nodes of $E(r, \varphi, t) = P\exp(i\phi)$, which involves the parameterization of (r, φ) coordinates by t. Of course, the approach is not ideal, especially in regions where the rings appear flat on the transverse plane. Around such special regions, the missing data points need to be added manually, but otherwise, this approach is mostly efficient and accurate.

I start with rearranging the terms of $E(r, \varphi, t) = P\exp(i\phi)$ into the following form:

$$\frac{r^2\,(1 + it + i\cos 2\varphi(d/2 + i\cos 2\epsilon))}{((1+it)^2 + (d/2 + i\cos 2\epsilon)^2)} = \ln\left|\frac{1}{P}\frac{\sin 2\epsilon}{\sqrt{(1+it)^2 + (d/2 + i\cos 2\epsilon)^2}}\right| - i\phi \tag{3.9}$$

To simplify the notation, I introduce the function $F(t) = -f(t)\left(\ln\left|P\sqrt{f(t)}/\sin 2\epsilon\right| + i\phi\right)$ where $f(t) = (1+it)^2 + (d/2 + i\cos 2\epsilon)^2$. The simplified version of (3.9) is then:

$$r^2\left(1 + it + i\cos 2\varphi(d/2 + i\cos 2\epsilon)\right) = F(t) \tag{3.10}$$

Now, to separate the terms r^2 and $\cos 2\varphi$, (3.10) is split into the real and imaginary parts, creating the following system of equations:

$$r^2(1 - \cos 2\varphi\cos 2\epsilon) = \operatorname{Re} F(t) \tag{3.11}$$

$$r^2(t + d/2\cos 2\varphi) = \operatorname{Im} F(t) \tag{3.12}$$

Solving for the system, r^2 and $\cos 2\varphi$ can be easily expressed in terms of t, resulting in the following parameterization:

$$r(t) = \sqrt{\frac{d/2\operatorname{Re}(F) + \cos 2\epsilon\operatorname{Im}(F)}{d/2 + t\cos 2\epsilon}} \tag{3.13}$$

$$\varphi(t) = \frac{1}{2}\arccos\left(\frac{\operatorname{Im}(F) - t\operatorname{Re}(F)}{d/2\operatorname{Re}(F) + \cos 2\epsilon\operatorname{Im}(F)}\right) \tag{3.14}$$

Using this method, I can use an array of sample points in t and calculate (r, φ), either real-valued, which corresponds to the location of the ring, or complex-valued, where the rings do not exist. By sorting for only the real-valued coordinates and following the quadrupole symmetry $(\pm x, \pm y) = (\pm r\cos\varphi, \pm r\sin\varphi)$, the coordinates of the vortex lines can be obtained. The above-mentioned special regions, where the algorithm may not work as well, are mostly around points where the rings arrange flatly. Two issues arise from that. If a ring bends and slightly flattens, sampling not small enough may fail to capture the coordinates of the ring. However, if the ring appears completely flat on a particular transverse plane, the algorithm may either detect only the four points calculated according to the algorithm, or miss the ring entirely.

The latter is the case with $t = t_*$ plane in elliptic and elliptic-astigmatic beams, where the rings are completely flat, occupying the whole perimeter of the spheroid on the transverse plane. The ring lies on the ellipse described by $|E(x, y, t_*)| = P$, so I can use it to calculate the missing coordinates of the ring. In astigmatic beams, no flat rings are possible.

Another two special regions where the method may come short are on $x = 0$ and $y = 0$ planes, and very close to the optical axis. The rings bend and flatten on $x = 0$ and $y = 0$ planes; this may be remedied by increasing the sample size in t, but that approach usually comes with a large computational cost. A more effective method is to calculate the missing points separately by solving for $\cos 2\varphi = \pm 1$ numerically. Essentially, I am looking for specific points of t where the parametrized angle $\varphi(t)$ hits either 0 or $\pi/2$, which correspond to points lying on $x = 0$ or $y = 0$.

When it comes to rings situated very close to the optical axis, however, there is no analytical method of calculating missing points. Such rings, due to their small size, also appear flat. To capture the whole ring, the sample size in t around the ends of spheroids must be increased. With all of the methods combined, vortex rings can finally be visualized, results presented in Fig. 12.

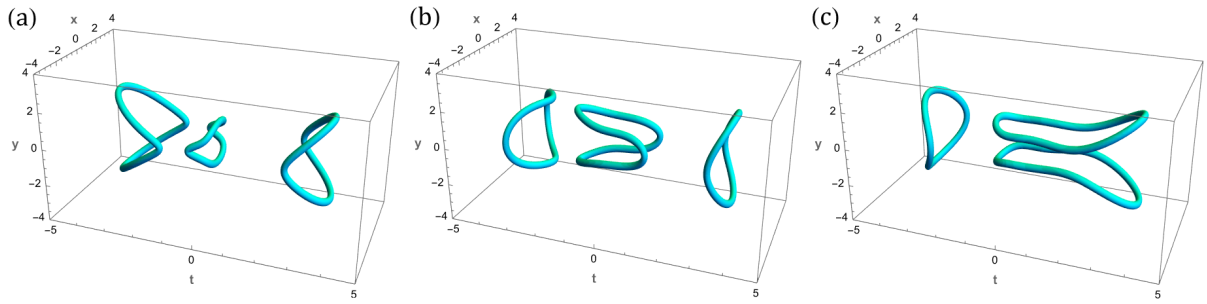

Figure 12: Vortex rings in (a) elliptic beam $\epsilon = \pi/5$, (b) astigmatic beam $d = 1$ and (c) elliptic-astigmatic beam $\epsilon = \pi/5, d = 1$ for $P = 1/5, \phi = -0.03\pi$.

The aforementioned algorithm is effective in visualizing rings, but provides no information on the topological charge. It was already established that the vortices in the system either have a $m = +1$ or $m = -1$ charge. Analyzing phase profiles at the transverse planes reveals a pattern: in the case of four roots, vortices situated on the same diagonal rotate in the same direction. A visual representation of such is presented in the Fig. 13.

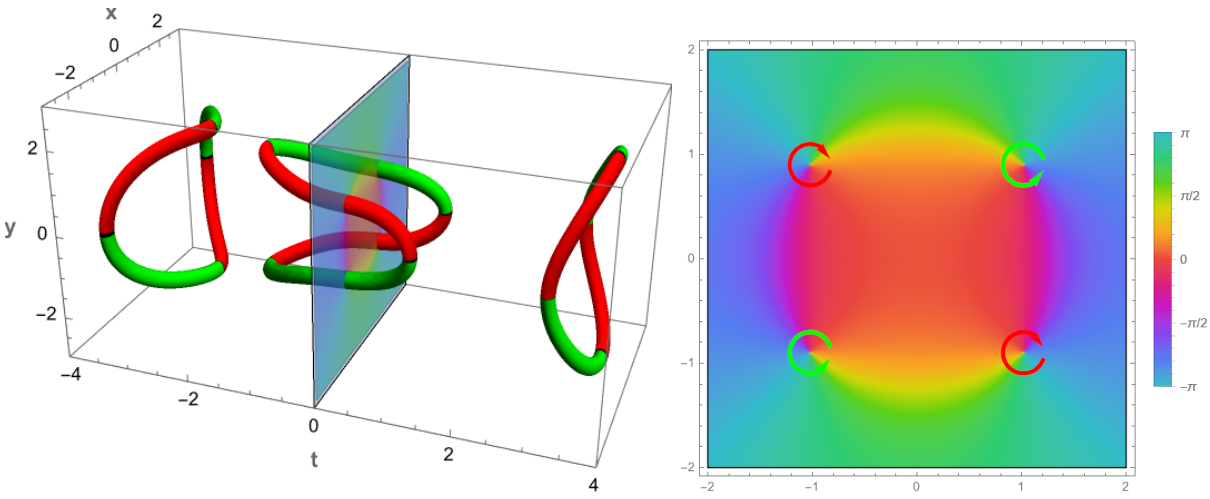

Figure 13: Vortex lines in the astigmatic beam $d = 1$ for $P = 1/5, \phi = -0.03\pi$ with the topological charge $m = +1$ (green) and $m = -1$ (red) and the cross section of the phase profile at the transverse plane $t = 0$.

Each vortex line situated at a certain quadrant of a transverse plane obtains a charge: positive if in the first and third quadrants and negative if otherwise. This is the result of the aforementioned quadrupole symmetry. Upon closer inspection, the points at $x = 0$ and $y = 0$ act as an annihilation point of the counter-rotating pair of vortex lines. In some

literature, such pairs are also referred to as vortex-antivortex pairs. A short reformulation into the vortex-antivortex framework is provided in appendix II.

This feature can be classified as a type of topological reaction in some sense; similar to the mutual nucleation/annihilation of the counter-rotating pair of rings in radial beams, the vortex-antivortex pair nucleates or annihilates at a point. However, I do not consider it as such in the scope of this thesis. Instead, I focus on the two fundamental types of events, the elliptic and the hyperbolic, which are both present in the system.

3.3 Topological events

In the radially symmetric beams, two types of vortex ring transformation are possible: the birth/death of a single ring on axis and the mutual nucleation/annihilation of a counter-propagating pair. The latter is a product of radial symmetry, and in elliptic beams, it is no longer possible. Instead, it decomposes into two separate reactions - the birth/death of a pair and reconnection. To structure the discussion, I categorize events into two types: on-axis and off-axis.

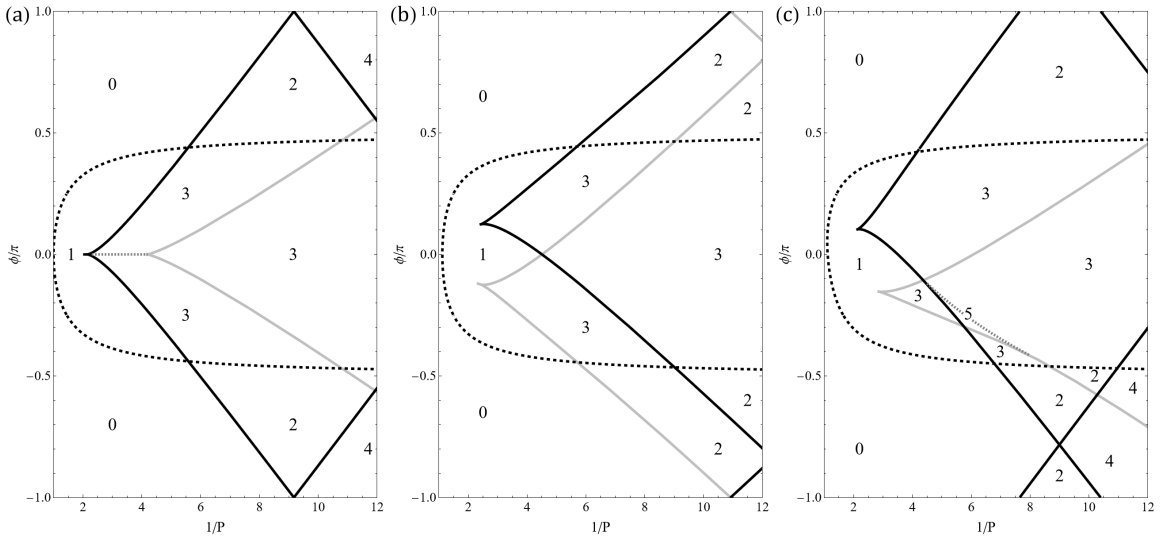

Figure 14: Numbers of vortex rings in the parameter domains separated by different topological events located on the optical axis $r = 0$ (dashed lines), in $x = 0$ plane (solid black lines) and in $y = 0$ plane (solid gray lines). Dotted lines in (a) and (c) indicate reconnections with a flat ring at $t = t_*$.

The on-axis event is the nucleation of a single ring. The mechanism is the same as in the radial case: as the phase iso-surface of $\arg E(x, y, t) = \phi$ crosses the spheroid described by $|E(x, y, t)| = P$, a ring appears on the point of intersection at $r = 0$. There is, unfortunately, no analytical expression for single-ring nucleation points, and they are mostly determined numerically. In elliptic and astigmatic beams, the t reversal symmetry ensures that if a ring is nucleated on a certain t_i, then it annihilates on $-t_i$, but that is not the case in elliptic-astigmatic beams. Such events always change the number of rings by 1. In Fig. 14, the on-axis events are marked by the dashed black line; anywhere on

the diagram, the line separates regions with the number of rings differing by 1.

When it comes to off-axis events, there are two distinct ones: the nucleation of a pair and reconnection, both marked by solid black and gray lines in Fig. 14. If in the radially symmetric beams, the off-axis event happened at the intersection of the spheroid and the hyperboloid of the beam radius, it is not the case here. Instead, the plane of intersection lies somewhere in between the two planes where these events occur. To distinguish between the two events, the phase at spheroids must be analyzed, since the topological reactions happen at the critical points.

To uncover all different types of reactions, manually checking critical points at all possible values of P is not very productive. Instead, a more appropriate approach would be to calculate the extremum points of $\psi(x,0,t)$ and $\psi(0,y,t)$ for a continuous range of P and $\phi \in [-\pi,\pi]$. To do so, I set $E(x,0,t) = P\exp(i\phi)$ and $E(0,y,t) = P\exp(i\phi)$, which lets me to easily separate x and y terms in each in the following way:

$$x^2 = S_x(t) = (2\cos^2\epsilon + i(t-d/2))\left(\ln\left|\frac{\sin 2\epsilon}{P\sqrt{f(t)}}\right| - i\phi\right) \tag{3.15a}$$

$$y^2 = S_y(t) = (2\sin^2\epsilon + i(t+d/2))\left(\ln\left|\frac{\sin 2\epsilon}{P\sqrt{f(t)}}\right| - i\phi\right) \tag{3.15b}$$

To map the critical points of (3.15a) and (3.15b) onto the (P,ϕ) parameter domain, I construct a system of equation where $\partial_t = \partial/\partial t$:

$$\begin{cases} \operatorname{Im} S_{x,y} = 0 \\ \partial_t \operatorname{Im} S_{x,y} = 0 \end{cases} \tag{3.16}$$

Here, P and ϕ can be easily separated and expressed in terms of t and ϵ, d. So by setting specific beam parameters ϵ, d and a range of sample points in t, I can uncover the bifurcation lines that indicate topological reaction on $x=0$ and $y=0$ planes, which are then can be mapped onto the (P,ϕ) parameter space, as in Fig. 14.

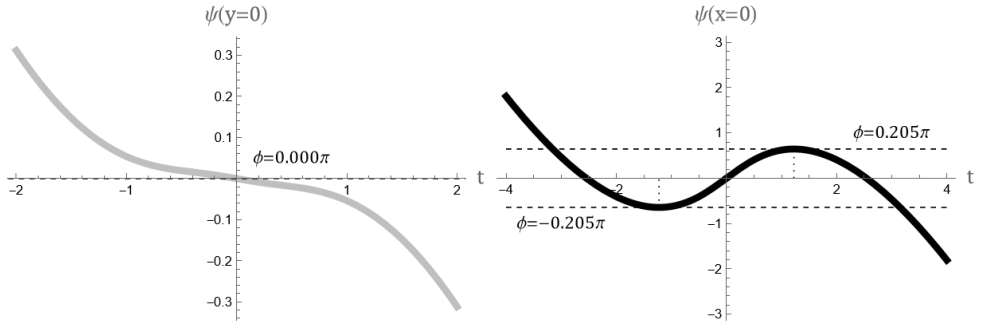

Figure 15: Phase $\psi(x,0,t)$ (gray) and $\psi(0,y,t)$ (black) at the spheroid $P = 1/4$ in the elliptic beam $\epsilon = \pi/5$.

Now, specific cases can be considered. Starting with the elliptic beam, I first consider

rings generated for $P = 1/4$ in $\epsilon = \pi/4$; the phase at spheroids is presented in Fig. 15.

The curves in Fig. 15 follow the $t \to -t$ symmetry as consistent with the beam shape in Fig. 11(a), which must also be accompanied by $\phi \to -\phi$ here. The event that happens on (t_i, ϕ_i) repeats for $(-t_i, -\phi_i)$. The phase at $x = 0$ is also different from the one on $y = 0$, which is a consequence of differing diffraction rates at each plane. In Fig. 15, the phase has two extremum points for $\psi(x = 0)$ at $\phi = \pm 0.205\pi$, which correspond to ϕ at which the number of rings changes by 2 in Fig. 14(a), signifying the birth of two rings.

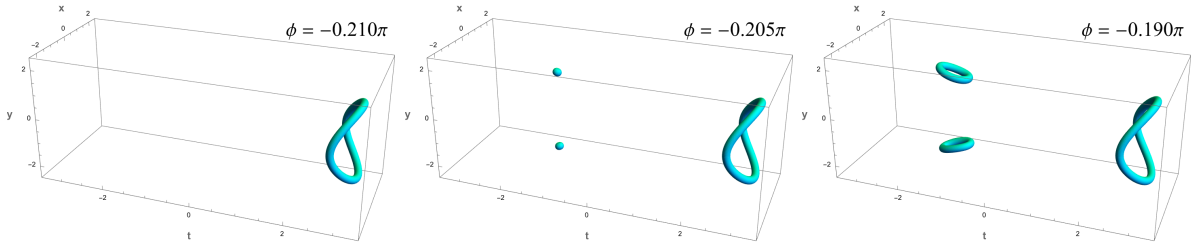

Figure 16: Nucleation of a pair of rings in elliptic beam $\epsilon = \pi/5$ at $P = 1/4$. The phase at nucleation corresponds to the largest critical point in Fig. 15.

In Fig. 14(a), for $P = 1/4$, there is a dotted bifurcation line of events at $t = t_*$, which in this case corresponds to a reconnection with a flat ring. This is a special type of topological reaction that only happens if $\epsilon \neq \pi/4$. At a plane of symmetry $t = t_*$, which is the focal plane $t = 0$ in this case, the ring is forced into the flat configuration, and so the rings can reconnect and fuse into one large vortex structure with a flat ring in the middle, as presented in the Fig. 17.

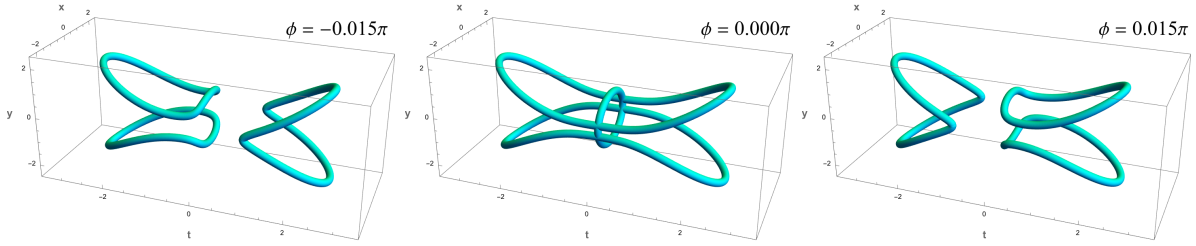

Figure 17: Reconnection of rings in elliptic beam $\epsilon = \pi/5$ at $P = 1/4$. The phase at reconnection corresponds to the inflection point in Fig. 15.

Now, for $P = 1/5$ in Fig. 14(a), there is a gray bifurcation line of events at $y = 0$ that spans $P > 1/4.2$ instead of the dotted one. In this case, the phase at $y = 0$ also has two extremum points, which results in $2 \to 2$ reconnection, presented in Fig. 19.

In astigmatic beams, the $t \to -t$ symmetry does not hold unless $d \to -d$. The shapes of solid bifurcation lines of events at $x = 0$ and $y = 0$ in 11(b) follow this reversal symmetry. This means that a reaction that occurs on $x = 0$ at a certain (t_i, ϕ_i) will repeat on $y = 0$ at $(-t_i, -\phi_i)$, and vice versa. If in elliptic beams the pair of rings would nucleate on $x = 0$ and reconnect on $y = 0$; here, both events can interchange planes according to the beam symmetry.

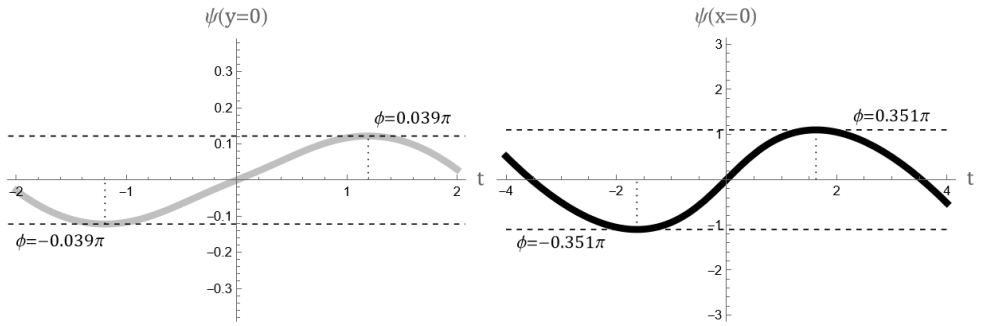

Figure 18: Phase $\psi(x,0,t)$ (gray) and $\psi(0,y,t)$ (black) at spheroid $P=1/5$ in the elliptic beam $\epsilon=\pi/5$.

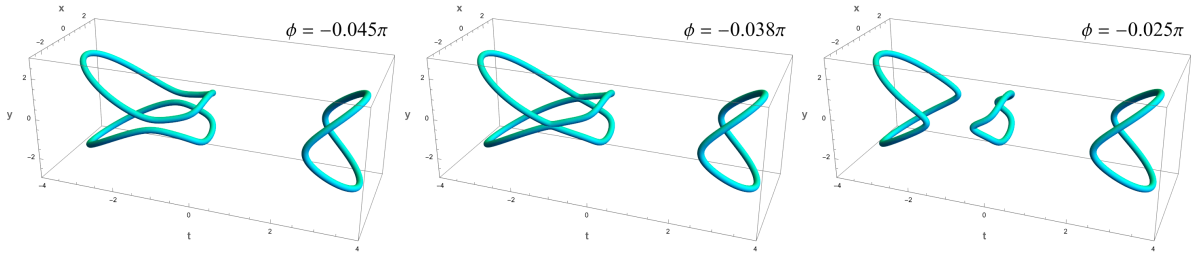

Figure 19: Reconnection of rings in elliptic beam $\epsilon=\pi/5$ at $P=1/5$. The phase at reconnection corresponds to the smaller critical point in Fig. 18.

I consider the astigmatic beam $d=1$ and a plane wave amplitude $P=1/4$. As stated previously, flat rings cannot appear in astigmatic beams. However, a unique $3\to 1$ reconnection as in Fig. 22 is possible, thanks to the perpetual ring deformation.

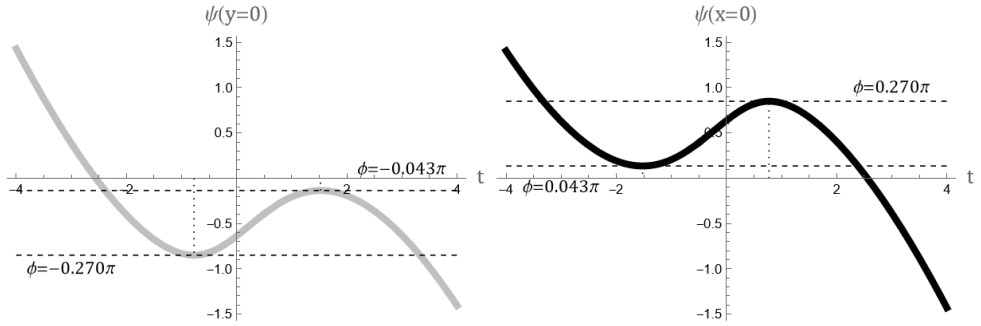

Figure 20: Phase $\psi(x,0,t)$ (gray) and $\psi(0,y,t)$ (black) at spheroid $P=1/4$ in the astigmatic beam $d=1$.

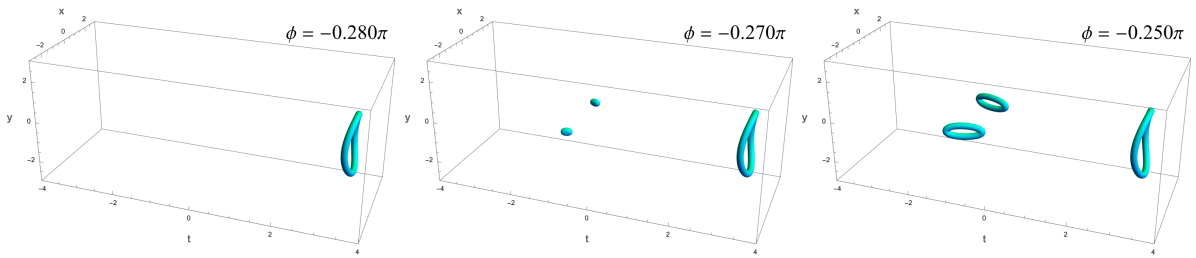

Figure 21: Nucleation of a pair of rings in astigmatic beam $d=1$ at $P=1/4$. The phase at nucleation corresponds to the largest critical point in Fig. 20.

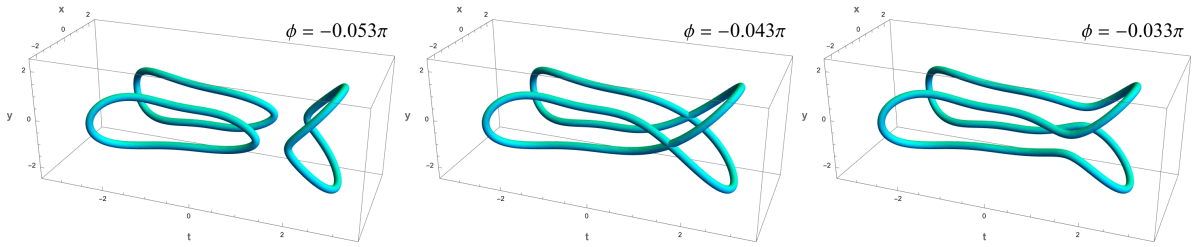

Figure 22: Reconnection of rings in astigmatic beam $d = 1$ at $P = 1/4$. The phase at reconnection corresponds to the smaller critical point in Fig. 20.

And finally, I consider the elliptic-astigmatic beam $\epsilon = \pi/5, d = 1$ at $P = 1/5$. The $t \to -t$ symmetry is broken, so the phase curves are also asymmetric.

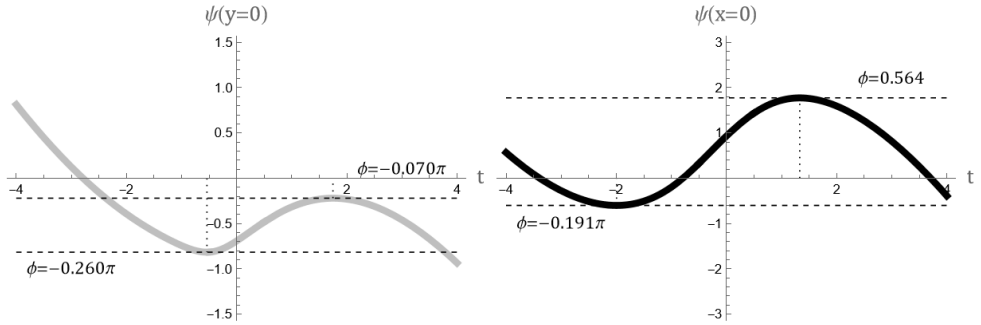

Figure 23: Phase $\psi(x, 0, t)$ (gray) and $\psi(0, y, t)$ (black) at spheroid $P = 1/5$ in the elliptic-astigmatic beam $\epsilon = \pi/5, d = 1$.

A similar pattern is noticeable in Fig. 11(c), where the bifurcation line of events at $x = 0$ is vastly different from the line of events at $y = 0$. Due to astigmatism, the nucleation of a pair can also happen on either $x = 0$ and $y = 0$, as well as reconnection.

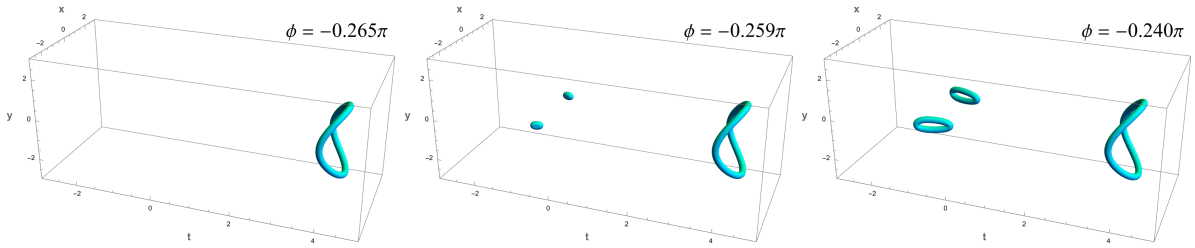

Figure 24: Nucleation of a pair of rings in elliptic-astigmatic beam $\epsilon = \pi/5, d = 1$ at $P = 1/5$. The phase at nucleation corresponds to the largest critical point on $y = 0$ in Fig. 20.

Similar to the elliptic case, there is a special range of P where a reconnection with a flat ring is possible. Moreover, the reconnection not only fuses the rings into one large structure but also allows for an additional pair of rings to appear briefly, resulting in a special $4 \to 2$ reconnection that cannot be achieved otherwise.

With that, I can conclude the discussion on topological events. But as mentioned previously, here I only considered beams that deviate from the radial symmetry only slightly; with heightened ϵ, d comes a growing complexity of topological maps in Fig. 14.

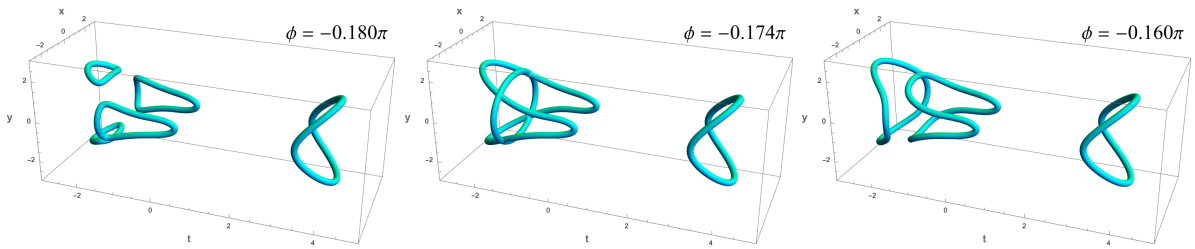

Figure 25: Reconnection of rings in elliptic-astigmatic beam $\epsilon = \pi/5, d = 1$ at $P = 1/5$.

This issue is addressed in the next section, where I introduce catastrophes that affect the topological reactions.

4 CATASTROPHES OF TOPOLOGICAL EVENTS AND BEAM CAUSTICS OF ELLIPTIC GAUSSIAN BEAMS

In this section, which also consists of three parts, I explore the parameter space (ϵ, d) beyond what was presented previously.

First, I reformulate the superposition (2.18) into the conic form, splitting the equation into absolute value and argument parts. The conics are then analyzed by applying the catastrophe theory principles, which will provide a groundwork for introducing catastrophes.

Next, the focus is on the cusp catastrophe. After outlining the governing system of equations, I present how the cusp appears in the parameter space and affects the topological events. The effects of the cusp catastrophe on the beam's amplitude surfaces are analyzed, revealing how it manifests as an observable physical phenomenon.

Finally, a similar approach is applied to the butterfly catastrophe. In addition to that, I highlight some differences in how these two catastrophes manifest in the respective parameter spaces and, consequently, the physical world.

4.1 Conic equations

The conics are curves obtained from the intersection of a conical surface and a plane. The four basic conics include the circle, ellipse, parabola and hyperbola. Paying closer attention to the equations governing the Gaussian beam envelope, one may notice conics in several areas: circles and ellipses in the transverse plane and hyperbolas in the beam shapes, so it is only natural to analyze how these shapes change as the parameters are varied.

In this context, I define a general form of the conic equation:

$$\frac{x^2}{A(t)} + \frac{y^2}{B(t)} = 1 \tag{4.1}$$

Now, rearranging the terms in the absolute part $|E(x, y, t)| = P$ results in the conic equation of the following form:

$$\frac{x^2}{a_1 G(t)} + \frac{y^2}{b_1 G(t)} = 1, \tag{4.2}$$

where the terms a_1 and b_1 in semi-major and semi-minor axes are defined as:

$$a_1 = \frac{4\cos^4\epsilon + (t - d/2)^2}{2\cos^2\epsilon} \tag{4.3a}$$

$$b_1 = \frac{4\sin^4\epsilon + (t + d/2)^2}{2\sin^2\epsilon}, \tag{4.3b}$$

with a common term $G(t)$ involving P:

$$G(t;\epsilon,d,P)=\ln\left|\frac{\sin 2\epsilon}{P((4\cos^4\epsilon+(t-d/2)^2)(4\sin^4\epsilon+(t+d/2)^2))^{1/4}}\right| \tag{4.4}$$

In a similar manner, I reformulate the argument part $\arg E(x,y,t)=\phi$:

$$\frac{x^2}{a_2H(t)}+\frac{y^2}{b_2H(t)}=1 \tag{4.5}$$

Here, a_2 and b_2 are similar to a_1 and b_1, except for the denominator part, as defined below:

$$a_2=\frac{4\cos^4\epsilon+(t-d/2)^2}{t-d/2} \tag{4.6a}$$

$$b_2=\frac{4\sin^4\epsilon+(t+d/2)^2}{t+d/2} \tag{4.6b}$$

And the term $H(t)$ containing ϕ is:

$$H(t;\epsilon,d,\phi)=\phi+\frac{1}{2}\left(\tan^{-1}\frac{t-d/2}{2\cos^2\epsilon}+\tan^{-1}\frac{t+d/2}{2\sin^2\epsilon}\right) \tag{4.7}$$

It was already established multiple times that the vortex lines lie on the intersection of planes described by $|E(x,y,t)|=P$ and $\arg E(x,y,t)=\phi$. So it should not be surprising that the same exact approach can be applied here; to implement that, I set the semi-major and semi-minor axes of the two conics (4.2) and (4.5) equal to each other:

$$a_1G(t)=a_2H(t) \tag{4.8a}$$

$$b_1G(t)=b_2H(t) \tag{4.8b}$$

In these two equations, ϕ can be easily separated from $H(t)$ since it is simply added and is not intertwined with the rest of the terms. Thus, I can formulate characteristic equations of phase $\phi=f_1(t)$ and $\phi=f_2(t)$, describing phase profiles at $y=0$ and $x=0$ planes, respectively. The equations below present the explicit forms of $f_1(t)$ and $f_2(t)$.

$$\begin{aligned}f_1(t)=\frac{t-d/2}{2\cos^2\epsilon}\ln\left|\frac{\sin 2\epsilon}{P((4\cos^4\epsilon+(t-d/2)^2)(4\sin^4\epsilon+(t+d/2)^2))^{1/4}}\right|-\\-\frac{1}{2}\left(\tan^{-1}\frac{t-d/2}{2\cos^2\epsilon}+\tan^{-1}\frac{t+d/2}{2\sin^2\epsilon}\right)\end{aligned} \tag{4.9}$$

$$\begin{aligned}f_2(t)=\frac{t+d/2}{2\sin^2\epsilon}\ln\left|\frac{\sin 2\epsilon}{P((4\cos^4\epsilon+(t-d/2)^2)(4\sin^4\epsilon+(t+d/2)^2))^{1/4}}\right|-\\-\frac{1}{2}\left(\tan^{-1}\frac{t-d/2}{2\cos^2\epsilon}+\tan^{-1}\frac{t+d/2}{2\sin^2\epsilon}\right)\end{aligned} \tag{4.10}$$

These two equations are, in fact, simplified versions of $\psi(x, 0, t)$ and $\psi(0, y, t)$ and are a bit easier to analyze. Unfortunately, they cannot be simplified further without losing important information, especially when it comes to small changes that seem insignificant but result in dramatic shifts. To demonstrate the resemblance, I plot both $f_1(t)$ and $f_2(t)$ for the first case in section 3.2: elliptic beam $\epsilon = \pi/5$ at $P = 1/4$, which are the same curves as in Fig. 15.

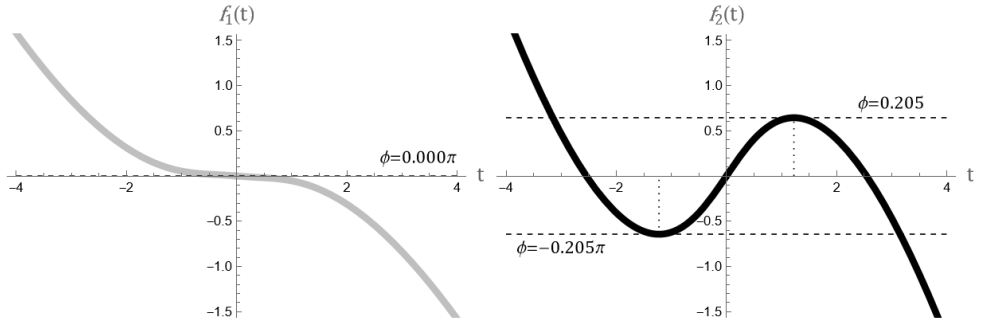

Figure 26: Characteristic phase $f_1(t)$ and $f_2(t)$ of the elliptic beam $\epsilon = \pi/5$ at $P = 1/4$.

One important aspect of these characteristic phase equations is that they turn into polynomial equations after the second derivative of t is taken. This helps identify singularity sets, uncovering catastrophes.

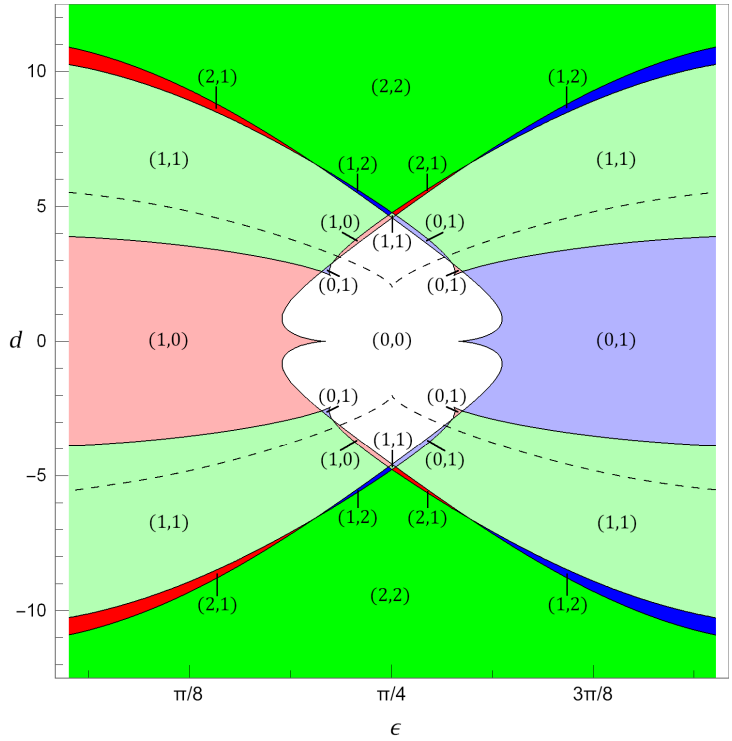

Figure 27: Domains with cusp and butterfly catastrophes in the parameter space (ϵ, d). The numbers in brackets indicate the numbers (0, 1, or 2) of butterfly catastrophes at, correspondingly, $(y = 0, x = 0)$ planes. Dashed lines separate the domain without cusp catastrophe (between the lines) from regions with one cusp (top and bottom).

Speaking of catastrophes, Fig. 27 presents the domains of cusp and butterfly catas-

trophes for $\epsilon \in (0, \pi/2)$ and $|d| < 12$. The process of calculating the lines separating the regions with and without the catastrophes is explained in more detail below.

4.2 The cusp

Previously, I emphasized the importance of characteristic phase equations, but here, I am not going to use them in full. That is because the cusp catastrophe concerns reactions on-axis; thus, a different, simpler approach is more suitable in this case.

The superposition on-axis is $E(0, 0, t) = P \exp(i\phi)$. Rearranging the terms results in the following:

$$i\phi = \ln \left| \frac{\sin 2\epsilon}{P\sqrt{(2\cos^2\epsilon + i(t - d/2))(2\sin^2\epsilon + i(t + d/2))}} \right| \tag{4.11}$$

Taking the absolute value of both parts yields the expression of characteristic phase on axis, which is simply $\phi = G(t)$. Now, to uncover the bifurcation points on the parameter space (ϵ, d) that introduce catastrophes, I take the first and second derivatives of $G(t)$:

$$\begin{cases} \partial_t G(t) = 0 \\ \partial_t^2 G(t) = 0 \end{cases} \tag{4.12}$$

The first derivative of $G(t)$ does not include the P term since it is cancelled out as a constant, leaving only t and beam shape parameters ϵ, d. Moreover, both of these equations are polynomials of degrees 3 and 4 in t, respectively, but the system cannot be solved analytically. The graphical solution is presented in Fig. 27 as a dashed line; the shape of the line in (ϵ, d) parameter space is what gives this catastrophe its name - the cusp.

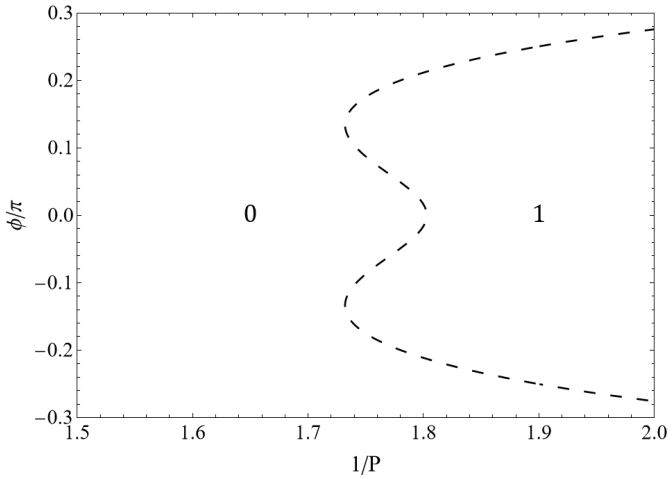

Figure 28: The number of vortex rings in the parameter domain (P, ϕ) separated by topological events located at the optical axis (dashed) for the astigmatic beam $d = 3$ with the cusp catastrophe.

In Fig. 14, the line representing reactions on-axis in (P, ϕ) parameter space appears to have a consistent shape, with one extremum around $\phi = 0$ and asymptotically extending to $\phi = \pm\pi/2$. For the beams with parameters (ϵ, d) in the regions with the cusp, however, that is not the case: the line now folds into itself, creating three extremums. In purely astigmatic beams, the catastrophe starts at $|d| = 2.0$, and when the ellipticity is introduced, it shifts up to $|d| = 5.6$.

There are two cases of how the cusp manifests in the system. The first is simple: the folding of a bifurcation line introduces an additional pair of points for the birth and death of a ring. A single ring appears on one end, disappears at a certain $t = t_i$ before reaching $t = 0$, appears again on $t = -t_i$ before disappearing completely on the other end.

As an example, I consider an astigmatic beam $d = 3$. In the parameter space (ϵ, d) in Fig. 27, that corresponds to the white region with the cusp but without the butterfly catastrophes. The snippet of (P, ϕ) parameter domain is presented in Fig. 28. Here, a single ring generated at $P = 1/1.8$ briefly disappears close to $t = 0$ and reappears on the other side.

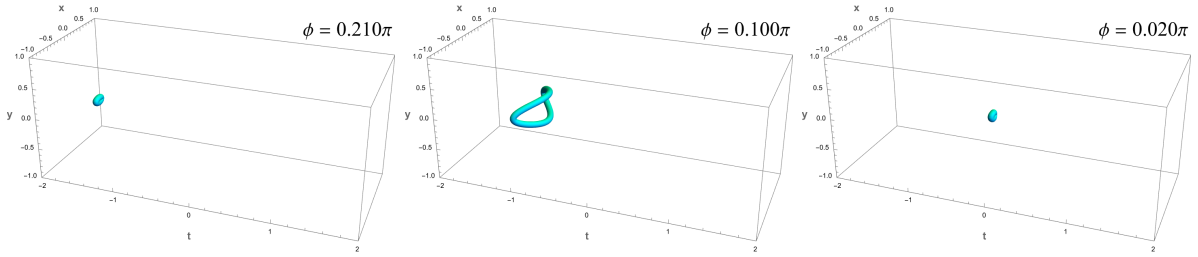

Figure 29: Vortex rings in the astigmatic beam $d = 3$ with the cusp catastrophe at $P = 1/1.8$.

This phenomenon of a ring disappearing and appearing again is obtained for $2.0 < |d| < 3.8$. At higher values of $|d|$, the reactions get more complicated: thanks to the interplay with the off-axis transformations, on-axis reconnection becomes possible.

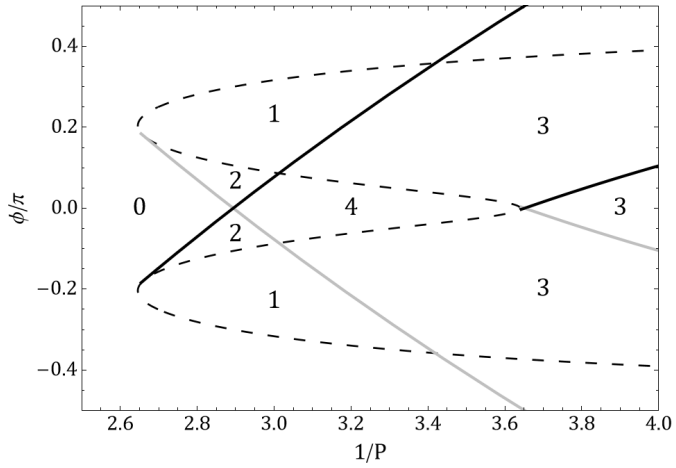

Figure 30: The number of vortex rings in the parameter domains (P, ϕ) separated by topological events located at the optical axis (dashed), at the $x = 0$ plane (black) and at the $y = 0$ plane (grey) for the astigmatic beam $d = 7$ with the cusp catastrophe.

To observe this reaction, a pair of rings must be generated off-axis first. Here I consider the astigmatic beam $d = 7$, which is inside the green region with cusp and double butterfly catastrophes in both $x = 0$ and $y = 0$ in Fig. 27. The dashed and solid bifurcation lines on the (P, ϕ) parameter space, presented in Fig. 30, are now interconnected thanks to the effects of the catastrophe.

The reconnection itself is presented in Fig. 31. However, an important note is that for the on-axis reconnection, the presence of the butterfly is not required. For example, in astigmatic beams, that covers a short range of d in $3.8 < |d| < 4.6$.

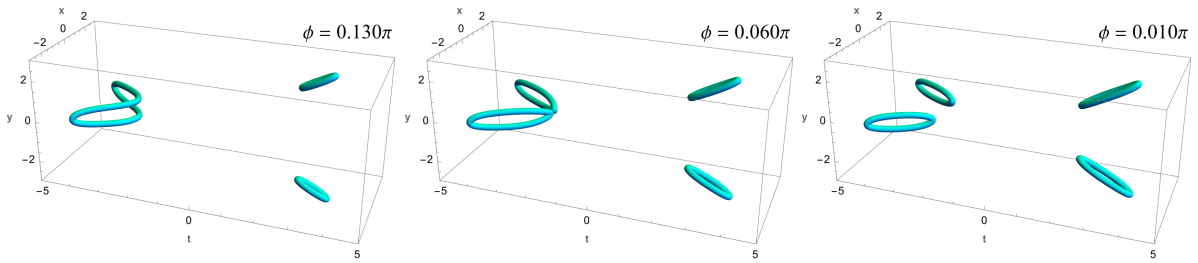

Figure 31: Vortex rings in the astigmatic beam $d = 7$ with the cusp catastrophe at $P = 1/3.2$.

The cusp catastrophe is exclusive to the events on the optical axis, and the reason behind its formation is quite intuitive. The region without the cusp in the (ϵ, d) parameter space spans $0 < |d| < 2$, no matter the value of ϵ. This hints that the cause behind the cusp catastrophe lies in heightened focal plane separation. Indeed, considering the amplitude iso-surfaces of the astigmatic beam $d = 3$ as in Fig. 32, the surface separates into two. This is in line with the fact that the rings can only appear on the corresponding amplitude iso-surface; so if the surface separates, the rings undergo reconnection or disappear, unable to propagate further.

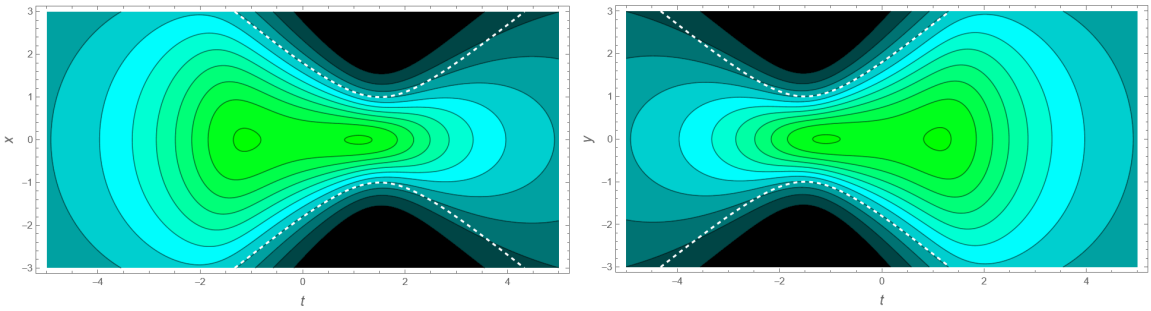

Figure 32: Contours of amplitude iso-surfaces $|E| = P$ of astigmatic beam $d = 3$ with the cusp catastrophe, and the beam radius (white dashed line).

Comparing the caustic surfaces of beams with and without the catastrophe makes it easier to visualize this effect. The surface of an astigmatic beam without the cusp catastrophe, presented in Fig. 33, seems only slightly deformed from the spheroid of a radially symmetric beam. Whereas the caustic surfaces of the astigmatic beam with the cusp catastrophe are visibly separated.

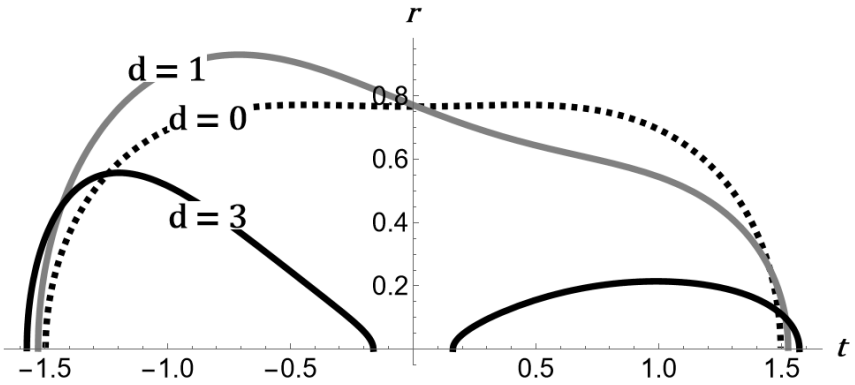

Figure 33: Contours of amplitude iso-surfaces $|E(x,0,t)| = P$ for $P = 1/1.8$ of a radially symmetric beam (dotted), beam without the cusp catastrophe (gray) and with the cusp catastrophe (black).

The mechanism behind the cusp catastrophe is straightforward and easily noticeable. This is not the case for the butterfly catastrophe, which is discussed in more detail in the next part.

4.3 The butterfly

As explained previously in section 4, the butterfly catastrophe has a more complex geometry and consists of a whole family of shapes that are usually governed by four parameters. In this case, the parameters are (ϵ, d) of the beam shape and (P, ϕ) of the plane wave. To find the bifurcation points in the parameter space (ϵ, d), the characteristic phase equations $f_1(t)$ and $f_2(t)$ defined in (4.9) and (4.10) are utilized. Constructing the following system of equations:

$$\begin{cases} \partial_t^2 f_{1,2}(t;\epsilon,d,P) = 0 \\ \partial_t^3 f_{1,2}(t;\epsilon,d,P) = 0, \end{cases} \tag{4.13}$$

which are both polynomials of degrees 5 and 6, respectively. Moreover, there are two independent systems for $x = 0$ and $y = 0$ planes, since events on $x = 0$ are independent of events on $y = 0$. Also, since the relations are rather complicated, finding solutions analytically is not possible. The graphical solution is presented as black solid lines for both $f_1(t)$ and $f_2(t)$ in Fig. 27.

For the butterfly catastrophe, there is an interesting feature - it can appear twice. At $d = 0$, which corresponds to elliptic beams, only a single catastrophe can occur on either $x = 0$ starting at $\epsilon > \pi/3.44$ or $y = 0$ at $\epsilon < \pi/4.78$. At $\epsilon = \pi/4$ (astigmatic beams), the catastrophes are always paired, appearing simultaneously at both $x = 0$ and $y = 0$, which starts at $|d| > 4.76$. The double butterfly catastrophe can only be achieved at high values of $|d|$, since heightened ϵ can only create a single butterfly on either $x = 0$ or $y = 0$.

Butterfly catastrophes are always responsible for generating an additional pair of rings near the focal planes, although how this pair interacts with other rings varies. First, I

consider an elliptic beam $\epsilon = \pi/7$. The classic butterfly shape that manifests in (P, ϕ) parameter space can be observed in Fig. 34.

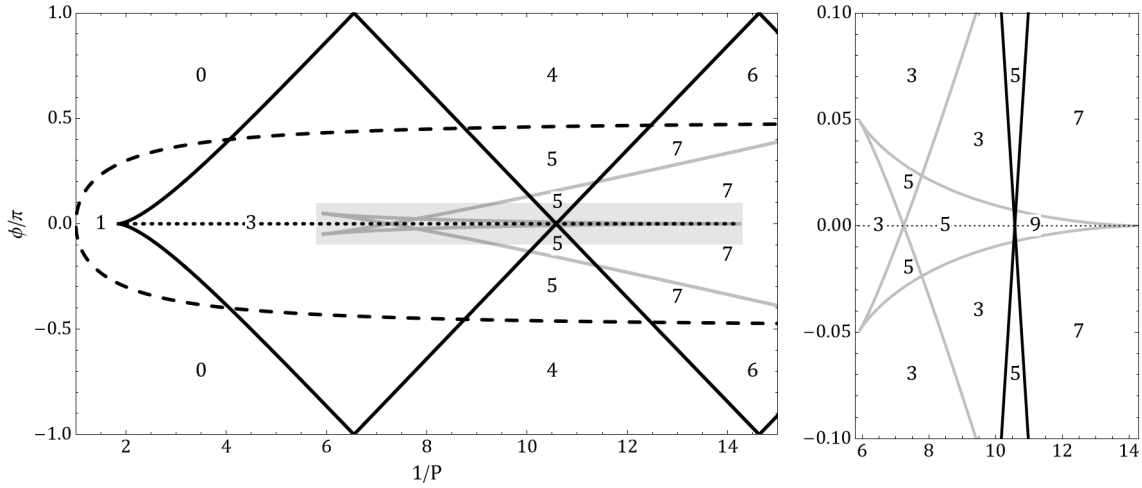

Figure 34: The number of vortex rings in the parameter domains (P, ϕ) separated by topological events located at the optical axis (dashed), at the $x = 0$ plane (black) and at the $y = 0$ plane (grey) for the elliptic beam $\epsilon = \pi/7$ with the butterfly catastrophe. Figure on the right magnifies the gray area on the left.

Depending on the specific part of the butterfly pattern, the dynamics of the rings vary. Near the two "cusps" of the butterfly in the range $6.0 < P < 7.2$ in Fig. 34, a single ring breaks into three: a large ring and a small pair near the focal plane $t = 0$, resulting in $3 \to 1$ reconnection. As ϕ changes, the pair quickly disappears, as presented in Fig. 35.

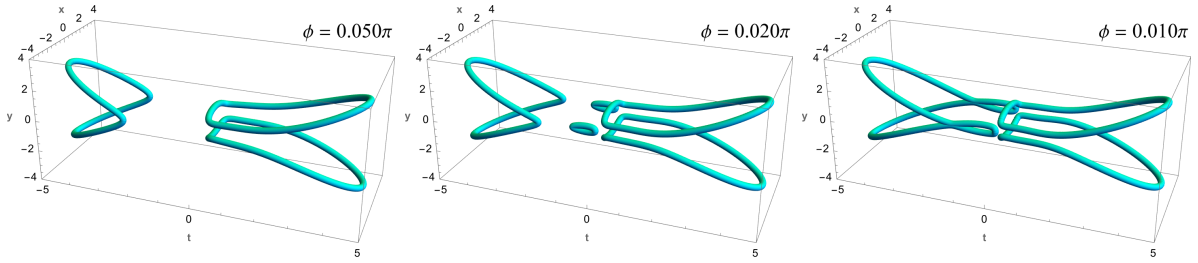

Figure 35: Vortex rings in the elliptic beam $\epsilon = \pi/7$ with the butterfly catastrophe at $P = 1/7$.

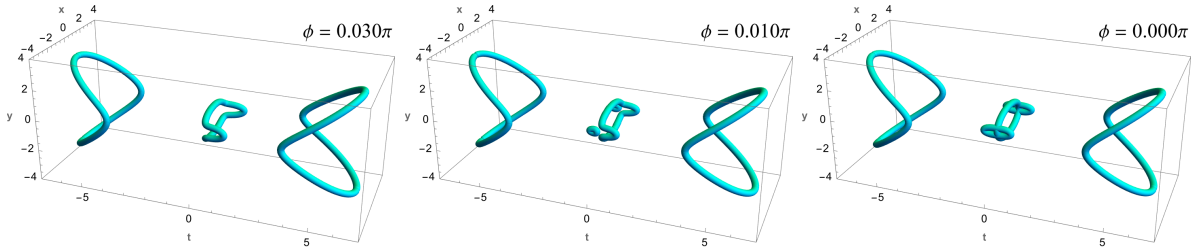

Figure 36: Vortex rings in the elliptic beam $\epsilon = \pi/7$ with the butterfly catastrophe at $P = 1/9$.

In the "tail" of the butterfly, which corresponds to the range $7.2 < P < 14$ in Fig. 34, an additional pair of rings near the focal plane $t = 0$ is also generated. However, there

is an important distinction between these two configurations. In the previous case, the pair reconnects with a large ring located several diffraction lengths away from the focal plane. Here, the pair reconnects exactly on the focal plane, forming a complex single ring with several connecting points. The pair here is also smaller compared to the first case, appearing as an unnoticeable feature next to larger and more prominent rings. An example of that is presented in Fig. 36.

For another example, I consider an astigmatic beam $d = 7$, which was already analyzed previously in regards to the cusp catastrophe. As in almost all astigmatic beams, there is a double butterfly in both $x = 0$ and $y = 0$ as indicated in Fig. 27. The way it manifests in the (P, ϕ) parameter space is presented in Fig. 37, with the first pair of butterflies existing in the range $1/4.3 < P < 1/4.7$ and the other in $1/42 < P < 1/52$.

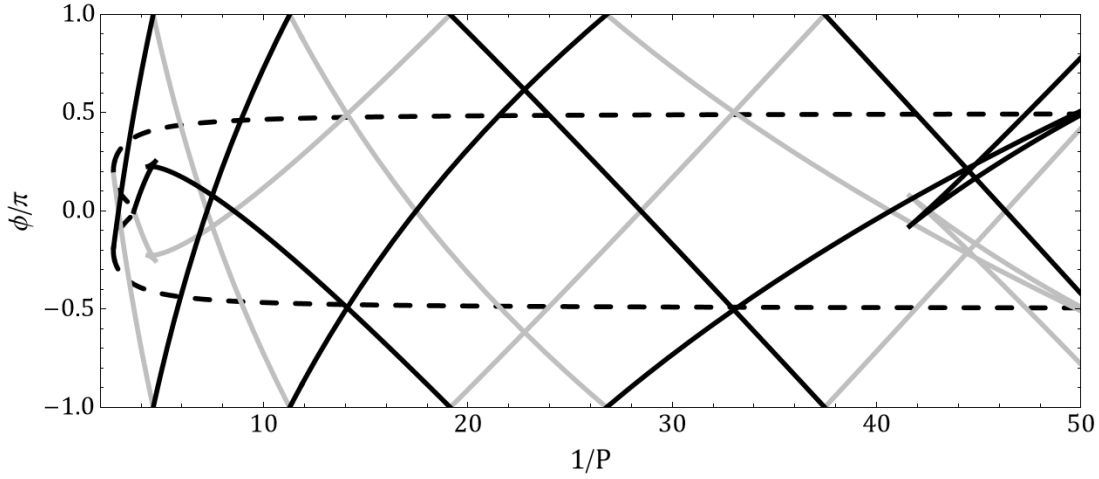

Figure 37: Topological events located at the optical axis (dashed), at the $x = 0$ plane (black) and at the $y = 0$ plane (grey) for the astigmatic beam $d = 7$ with double butterfly catastrophes on both $x = 0$ and $y = 0$.

Analyzing only the first pair of butterflies is sufficient, since the second pair affects the system similarly: by generating an additional pair of rings. Fig. 38 presents a snippet of Fig. 37 with the first two butterflies, showcasing how they change the number of rings.

Crossing the butterfly here yields the same result as in Fig. 35: a pair of rings is generated, reconnecting with the nearby larger ring in a short range of ϕ. But one may notice an interesting feature - very close to the intersection of the bifurcation lines of the butterfly, which is around $P = 1/4.55$, a $5 \to 1$ reconnection can be achieved.

As mentioned previously, butterfly catastrophes always generate an additional pair of rings near the focal planes; however, what exactly causes these catastrophes to appear is not very obvious. Butterfly catastrophe, similar to the cusp catastrophe, is the result of amplitude iso-surface deformation, but in a completely different way.

Drawing attention to Fig. 40, one may notice that the surfaces are smooth and do not discontinue near the symmetry planes $t = 0$ as it does with the cusp. The caustic surfaces resemble the general shape of spheroids in the radially symmetric beams, but noticeably differ around the focal planes.

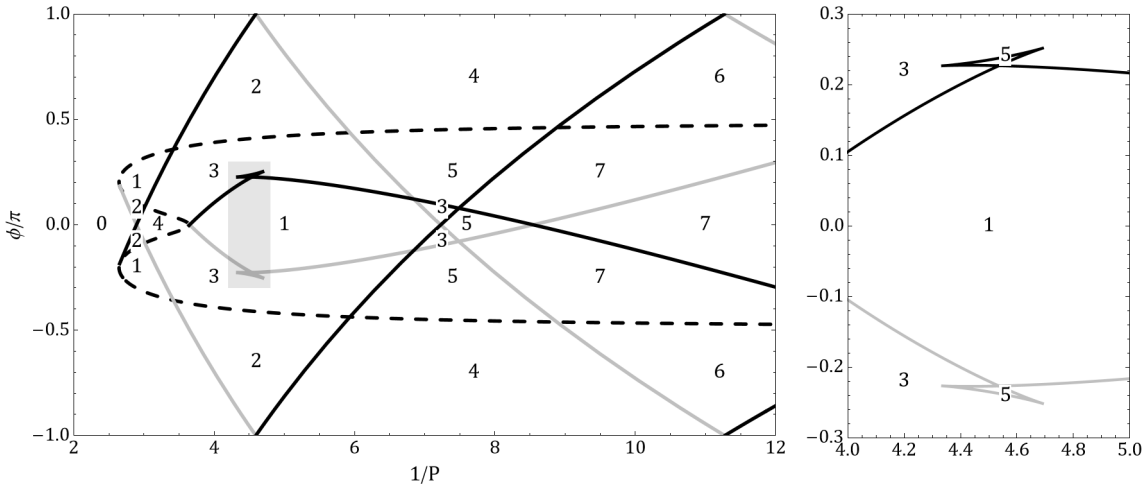

Figure 38: The number of vortex rings in the parameter domains (P, ϕ) separated by topological events located at the optical axis (dashed), at the $x = 0$ plane (black) and at the $y = 0$ plane (grey) for the astigmatic beam $d = 7$ with the butterfly catastrophe. Figure on the right magnifies the gray area on the left.

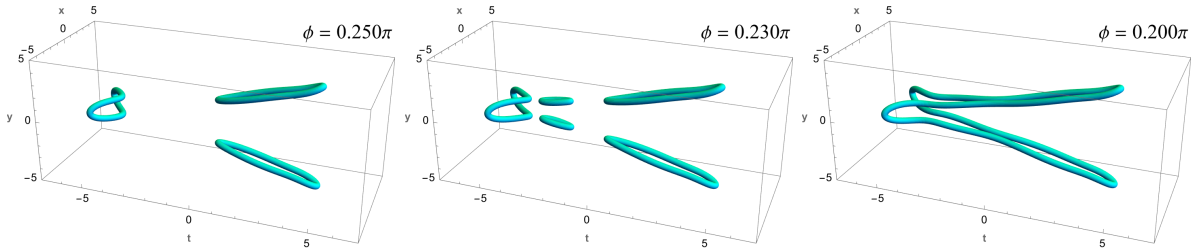

Figure 39: Vortex rings in the astigmatic beam $d = 7$ with the butterfly catastrophe at $P = 1/4.5$.

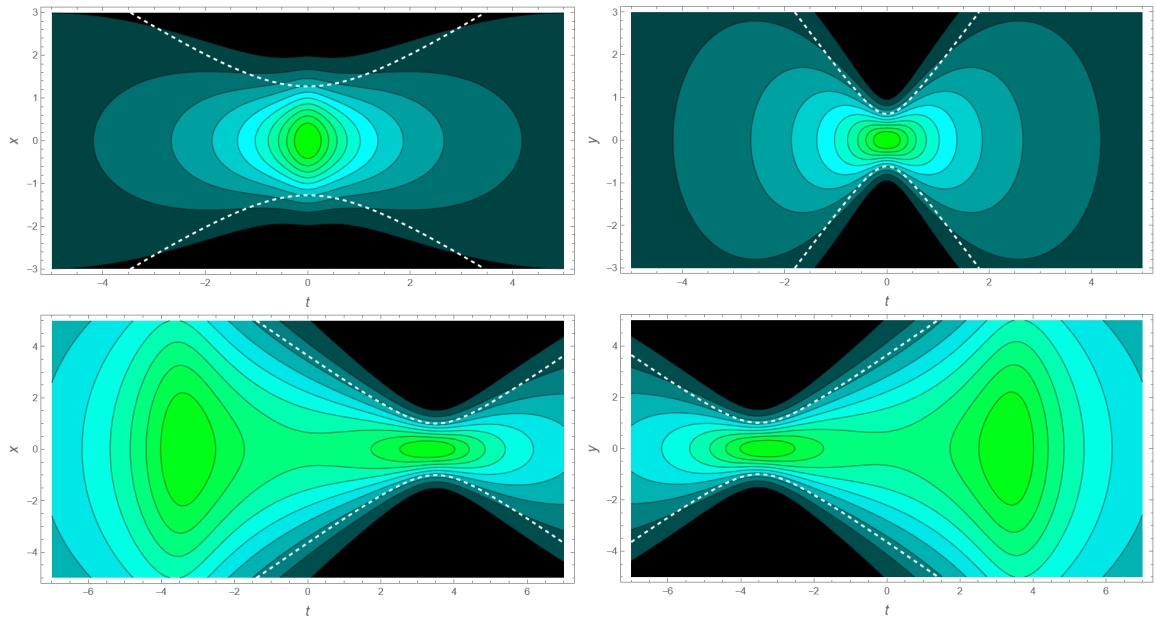

Figure 40: Contours of amplitude iso-surfaces $|E| = P$ of elliptic beam $\epsilon = \pi/7$ (top) and astigmatic beam $d = 7$ with the butterfly catastrophe, and the beam radius (white dashed line).

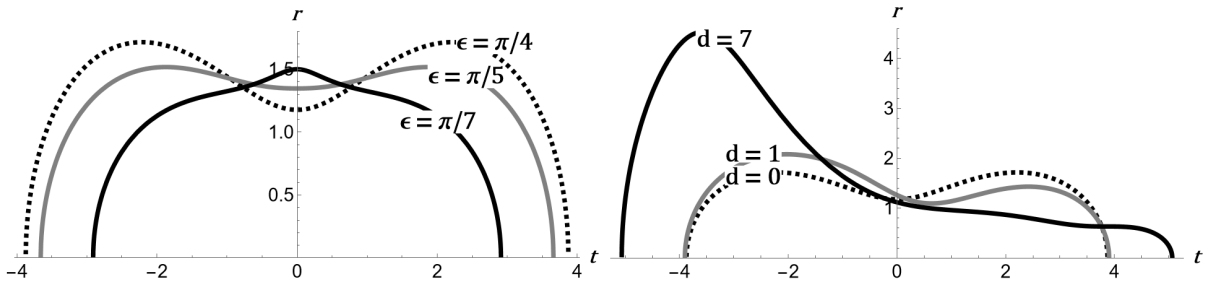

Figure 41: Contours of amplitude iso-surfaces $|E(x, 0, t)| = P$ for $P = 1/4$ of radially symmetric beams (dotted), beams without the butterfly catastrophe (gray) and with the butterfly catastrophe (black).

Near the symmetry plane $t = 0$ in the elliptic beam in Fig. 41, the surface along the x-axis curves outwards instead of inward. Similar behavior can be noticed in the astigmatic beam, where the spheroids, instead of having two prominent peaks resembling a dumbbell, have only one very large extremum at $t = -3.5$ and an almost unnoticeable second one at $t = 3.5$. Since the additional pair of rings is generated exactly near the focal planes, it is safe to claim that the butterfly catastrophe is the result of amplitude iso-surface deformation around the focal planes.

With that, I can conclude the discussion on catastrophes in elliptic Gaussian beams. The existence of such nuanced events in this system is surprising, however, it demonstrates that complex phenomena can emerge even in relatively simple systems.

5 CONCLUSIONS

Vortex rings are an important subject in turbulent motion; a deeper understanding of their dynamics offers valuable insights into a broad spectrum of physical phenomena. In this thesis, I investigate the vortex rings and associated topological reactions in the superposition of the Gaussian beam and the plane wave. This system can be replicated in a laboratory setting using accessible equipment, providing a robust framework for studying vortex ring dynamics and topological transformations.

The Gaussian beam envelope is governed by the Schrödinger-type paraxial wave equation. The elliptic transverse profile of the beam is controlled by the ellipticity parameter ϵ, which regulates the beam waist radii in $x = 0$ and $y = 0$ planes, and the astigmatism parameter d, which stands for the distance of focal plane separation. At $\epsilon = \pi/4, d = 0$, the radially symmetric beam is recovered. The beams are categorized into three: the elliptic ($\epsilon \neq \pi/4, d = 0$), astigmatic ($\epsilon = \pi/4, d \neq 0$), and elliptic-astigmatic ($\epsilon \neq \pi/4, d \neq 0$). The plane wave is also defined by two parameters of relative amplitude P and relative phase ϕ.

The superposition creates vortex rings that are deformed in 3D space, except for the special planes in elliptic and elliptic-astigmatic beams where the rings can arrange flat on the transverse plane. Breaking the radial symmetry introduces new types of topological reactions into the system. In general, I distinguish two main types of topological events: the on-axis, which is the birth/death of a single ring, and off-axis, which are the nucleation of a pair of rings and reconnection. The configuration of rings and subsequent topological reactions differ according to the beam symmetry.

With heightened values of ϵ and d, the complexity of topological reactions increases, creating catastrophes. There are two types of catastrophes: the cusp and the butterfly, affecting on-axis and off-axis events, respectively. The cusp creates a pair of points where the single ring can appear or disappear; increasing d further allows for on-axis reconnection, which could not be achieved before. The butterfly always results in a small pair of rings generated off-axis, though how they interact with the rest of the rings varies case-by-case. Both types of catastrophes are a consequence of caustic surface deformation. The cusp results from the separation of amplitude iso-surfaces into two, whilst the butterfly is created due to deformation of surfaces near the focal planes.

The fundamental aim of this study is to advance the understanding of the fine structure of light. Despite its perceived simplicity, the system is rich in topological events; introducing tilted and rotating beams, which will break the underlying quadrupole symmetry, could result in even more complex types of topological reactions. A potential, albeit unrealistic, application would be to use this knowledge to design a system capable of creating vortex knots in a controlled manner. Nevertheless, a system of only four parameters exhibiting such complex topological phenomena is already remarkable in itself and holds potential for a variety of practical applications.

APPENDIX I: ROTATING ELLIPTIC GAUSSIAN BEAM

First, introducing a new principal coordinate system (X, Y) that allows for rotation. Here, (X, Y) can be defined as (x, y) rotated by an angle θ. The coordinate transformation matrix is then defined as:

$$\begin{bmatrix} X \\ Y \end{bmatrix} = \begin{bmatrix} \cos\theta & -\sin\theta \\ \sin\theta & \cos\theta \end{bmatrix} \begin{bmatrix} x \\ y \end{bmatrix} = \begin{bmatrix} x\cos\theta - y\sin\theta \\ x\sin\theta + y\cos\theta \end{bmatrix} \tag{I.1}$$

Variable θ introduces an additional degree of freedom. At fixed θ the beam is non-rotating, and by setting a specific value I can control the orientation of the beam. But also, by varying θ in time, the rotation can be achieved.

Now, simply solving for the (2.6) in the frame of principal coordinates results in the following rotating beam:

$$\begin{aligned} E(x,y,t) = {} & \frac{\sin 2\epsilon}{\left((4\cos^4\epsilon + (t)^2)(4\sin^4\epsilon + (t)^2)\right)^{1/4}} \times \\ & \times \exp\left[-\left(\frac{\cos^2\theta}{w_x^2(t)} + \frac{\sin^2\theta}{w_y^2(t)}\right) x^2 - \left(\frac{\sin^2\theta}{w_x^2(t)} + \frac{\cos^2\theta}{w_y^2(t)}\right) y^2 - \left(\frac{\sin 2\theta}{w_y^2(t)} - \frac{\sin 2\theta}{w_x^2(t)}\right) xy \right] \times \\ & \times \exp\left[i\left(\frac{\cos^2\theta}{R_x(t)} + \frac{\sin^2\theta}{R_y(t)}\right) x^2 + i\left(\frac{\sin^2\theta}{R_x(t)} + \frac{\cos^2\theta}{R_y(t)}\right) y^2 + i\left(\frac{\sin^2 2\theta}{R_x(t)R_y(t)}\right) xy \right] \times \\ & \times \exp\left[-\frac{i}{2}\left(\arctan\left[\frac{t-d/2}{2\cos^2\epsilon}\right] + \arctan\left[\frac{t+d/2}{2\sin^2\epsilon}\right] \right) \right] \end{aligned} \tag{I.2}$$

Here, the beam radii are in already familiar form:

$$w_x(t) = \sqrt{\frac{4\cos^4\epsilon + (t-d/2)^2}{2\cos^2\epsilon}} \tag{I.3a}$$

$$w_y(t) = \sqrt{\frac{4\sin^4\epsilon + (t+d/2)^2}{2\sin^2\epsilon}}, \tag{I.3b}$$

and the wavefront curvatures are:

$$R_x(t) = \frac{4\cos^4\epsilon + (t-d/2)^2}{t-d/2} \tag{I.4a}$$

$$R_y(t) = \frac{4\cos^4\epsilon + (t+d/2)^2}{t+d/2} \tag{I.4b}$$

APPENDIX II: VORTEX-ANTIVORTEX PAIRS

The governing equations of an optical field are formulated by using its "lighter" components, treating dark regions as mere voids. This approach is quite intuitive; light is directly observable and measurable, thus, it is only natural to describe the field in terms of quantities that are experimentally accessible. However, the focus can be inverted, and the field can be constructed from the dark parts too. In this context, vortices, where the field amplitude vanishes due to destructive interference, are at the forefront. The distribution of darkness in the field, i.e. trajectories of the vortices, can be treated as a skeleton, around which the light field is structured.

Here, I introduce new complex coordinates: $w = (x + iy)/\sqrt{2}$ and $\bar{w} = (x - iy)/\sqrt{2}$, which represent the field in terms of parts that rotate clockwise and anticlockwise. This allows for distinction between the counter-rotating vortex lines, which is more convenient than mapping the phase profiles and calculating the winding numbers.

Expressing the Schrödinger-type paraxial wave equation in terms of w and $\bar{w}$ can be achieved by simply implementing the chain rule:

$$\frac{\partial E}{\partial x} = \frac{\partial E}{\partial w}\frac{\partial w}{\partial x} + \frac{\partial E}{\partial \bar{w}}\frac{\partial \bar{w}}{\partial x} = \frac{1}{\sqrt{2}}\left(\frac{\partial E}{\partial w} + \frac{\partial E}{\partial \bar{w}}\right) \tag{II.1}$$

$$\frac{\partial E}{\partial y} = \frac{\partial E}{\partial w}\frac{\partial w}{\partial y} + \frac{\partial E}{\partial \bar{w}}\frac{\partial \bar{w}}{\partial y} = \frac{i}{\sqrt{2}}\left(\frac{\partial E}{\partial w} - \frac{\partial E}{\partial \bar{w}}\right), \tag{II.2}$$

and repeating the same process for the second derivatives:

$$\frac{\partial^2 E}{\partial x^2} = \frac{1}{2}\left(\frac{\partial^2 E}{\partial w^2} + \frac{\partial^2 E}{\partial \bar{w}^2}\right) + \frac{\partial^2 E}{\partial w \partial \bar{w}} \tag{II.3}$$

$$\frac{\partial^2 E}{\partial y^2} = -\frac{1}{2}\left(\frac{\partial^2 E}{\partial w^2} + \frac{\partial^2 E}{\partial \bar{w}^2}\right) + \frac{\partial^2 E}{\partial w \partial \bar{w}} \tag{II.4}$$

Plugging the final expressions into (2.14) from section 2 results in:

$$2i\frac{\partial E}{\partial t} + \frac{\partial^2 E}{\partial w \partial \bar{w}} = 0 \tag{II.5}$$

One can derive the complex scalar field $E(w, \bar{w}, t)$ from the paraxial wave equation (II.5). But since the solution is already expressed in (x, y), simply applying the coordinate transformation directly is enough. Thus the complex field $E(w, \bar{w}, t)$ is:

$$E(w, \bar{w}, t) = \frac{\sin 2\epsilon}{\sqrt{f(t)}} \exp\left(\frac{\cos 2\epsilon - id/2}{f(t)}(w^2 + \bar{w}^2) - \frac{2(1 + it)}{f(t)} w\bar{w}\right) \tag{II.6}$$

where $f(t) = (1 + it)^2 + (d/2 + i\cos 2\epsilon)^2$.

APPENDIX III: TILTED BEAMS

In this thesis, I have only considered the plane wave to be co-propagating. Returning to the radially symmetric beams, I can choose to tilt the plane wave; the direction of the tilt is along the positive x-axis $\vec{q} = q\hat{\imath}$ and $q > 0$. Finding the nodal lines of the superposition follows the same approach as previously, that is, separating amplitude and phase equations:

$$\begin{cases} |E(x,y,t)| = P, \\ \arg E(x,y,t) = qx - q^2 t/4 + \phi + 2\pi n, \end{cases} \tag{III.1}$$

Introducing the polar coordinates in transverse plane (r, φ), the latter transforms to $\arg E(r,t) = r^2 t/(1+t^2) - \tan^{-1} t$. The first of (III.1) describes amplitude iso-surfaces of the beam envelope and does not depend on the tilt of the plane wave q:

$$\rho(t) = \sqrt{-(1+t^2)\ln\left(P\sqrt{1+t^2}\right)}. \tag{III.2}$$

From the second of (III.1), two important relations can be derived. First, at the optical axis $r = 0$ for the endpoints of the spheroids $|t| = \sqrt{P^{-2} - 1}$, the dashed bifurcation line of reactions is obtained:

$$\phi = q^2 t_{\max}/4 - \tan^{-1} t_{\max} - 2\pi n. \tag{III.3}$$

Second, for $r \neq 0$, the azimuthal location of vortex lines is described by:

$$\cos\varphi = \frac{\rho}{q}\frac{t}{1+t^2} + \frac{q}{\rho}\frac{t}{4} - \frac{\tan^{-1} t + \phi + 2\pi n}{q\rho}, \tag{III.4}$$

The question now is where the solutions exist and how do they look like; condition $|\cos\varphi| \leq 1$ may give some boundaries in the parameter space (P, ϕ). But one claim can be made: there seem to be no flat rings.

PUBLICATIONS

Journal articles

1. Z. Kulchukova and A. Desyatnikov, "Vortex Ring Reconnections in Elliptic Gaussian Beams," Optics Letters **49**(4), 915-918 (2024).

Honors thesis

1. Z. Kulchukova, "Vortex Ring Reconnections in Paraxial Laser Beams," Department of Physics, School of Sciences and Humanities, Nazarbayev University (2023).

Conference talks

1. Z. Kulchukova, A. Ferrando and A. Desyatnikov, "Catastrophes in vortex rings reconnections," the 17th International Conference "Correlation Optics 2025", Chernivtsi, Ukraine, September 8-12, 2025.

2. Z. Kulchukova and A. Desyatnikov, "Spontaneous vortex rings in free-propagating and self-focused laser beams," 33rd Annual International Laser Physics Conference, Szeged, Hungary, June 30 - July 4, 2025.

3. Z. Kulchukova, A. Ferrando and A. Desyatnikov, "Optical vortex rings: reconnections and catastrophes," CLEO/Europe-EQEC 2025 Conference, Munich, Germany, June 23-27, 2025.

4. Z. Kulchukova and A. Desyatnikov, "Optical vortex rings," Fourth Annual Meeting of Kazakh Physical Society, Ust-Kamenogorsk, Kazakhstan, June 4–7, 2025.

5. Z. Kulchukova and A. Desyatnikov, "Vortex rings in free-propagating and self-focused laser beams," 3rd International Conference of Quantum, Nonlinear and Nanophotonics (ICQNN), Nottingham, UK, August 28 - September 2, 2024

6. Z. Kulchukova and A. Desyatnikov. "Topological transformations of vortex rings in paraxial laser beams," the 14th International Conference on Metamaterials, Photonic Crystals META 2024, Toyama, Japan, July 16-19, 2024.

7. A. Desyatnikov and Z. Kulchukova, "Vortex rings and ring reconnections in paraxial laser beams," the 4th International Conference on Optics, Photonics and Lasers OPL 2023, Hiroshima, Japan, December 4-7, 2023.

8. A. Desyatnikov and Z. Kulchukova, "Vortex rings reconnections in Gaussian laser beams," the 16th International Conference "Correlation Optics 2023", Chernivtsi, Ukraine, September 18-21, 2023.

REFERENCES

[1] C. Huygens, *Treatise on light* (Pieter van der Aa, Leiden, 1960).

[2] Y. Thomas, "The Bakerian Lecture. Experiments and calculations relative to physical optics," Philosophical Transactions of the Royal Society of London **94**, 1 (1804).

[3] J. Hecht, *Beam: the race to make the laser* (Oxford University Press, New York, 2005).

[4] J. Nishizawa, "Extension of frequencies from maser to laser," Proceedings of the Japan Academy, Series B **85**, 454 (2009).

[5] A. Einstein, "On the quantum theory of radiation," Physikalische Zeitschrift **18**, 121 (1917).

[6] T. Maiman, "Stimulated optical radiation in ruby," Nature **187**, 493 (1960).

[7] A. Schawlow and C. Townes, "Infrared and optical masers," Physical Review **112**, 1940 (1958).

[8] J. Gordon, H. Zeiger, and C. Townes, "The maser - new type of microwave amplifier, frequency standard, and spectrometer," Physical Review **99**, 1264 (1955).

[9] N. Basov and A. Prokhorov, "Theory of the molecular generator and molecular power amplifier," Soviet Physics Journal of Experimental and Theoretical Physics **3**, 560 (1956).

[10] A. Siegman, "Unstable optical resonators for laser applications," Proceedings of the IEEE **53**, 277 (1965).

[11] A. Siegman, *Lasers* (University Science Books, Palo Alto, 1986).

[12] J. Durnin, "Exact solutions for nondiffracting beams. I. The scalar theory," Optical Society of America **4**, 651 (1987).

[13] J. Foley and E. Wolf, "Note on the far field of a Gaussian beam," Optical Society of America **69**, 761 (1979).

[14] H. Kogelnik, "On the propagation of Gaussian beams of light through lenslike media including those with a loss or gain variation," Applied Optics **4**, 1562 (1955).

[15] A. Ferrando, A. Popiołek-Masajada, J. Masajada, R. Markevich, and A. Khoroshun, "Vortex-antivortex pair control in quadrupole Gaussian beams," Optics Express **31**, 23444 (2023).

[16] M. Kim, T. Scharf, C. Rockstuhl, and H. Herzig, *"Phase anomalies in micro-optics" Progress in optics, Volume 58E*, edited by E. Wolf (Elsevier, Amsterdam, 2013).

[17] R. Thom, *Structural Stability and Morphogenesis* (W. A. Benjamin, 1972).

[18] V. Arnol'd and G. Wassermann, *Catastrophe Theory, 3rd ed.* (Springer, 2003).

[19] E. Zeeman, *"Catastrophe theory," in Structural Stability in Physics*, edited by H. E. Werner Güttinger (Springer, 1979).

[20] H. Trinkaus and F. Drepper, "On the analysis of diffraction catastrophes," Journal of Physics A Mathematical and General **10**, L11–L16 (1977).

[21] J. Nye, *Natural focusing and fine structure of light: caustics and wave dislocations* (Institute of Physics Publishing, Bristol, 1999).

[22] M. Berry and C. Upstill, "Catastrophe optics: morphologies of caustics and their diffraction patterns," Progress in Optics **28**, 257 (1980).

[23] R. Höhmann, U. Kuhl, H.-J. Stöckmann, L. Kaplan, and E. J. Heller, "Freak waves in the linear regime: a microwave study," Physical Review Letters **104**, 093901 (2010).

[24] A. Mathis, L. Froehly, S. Toenger, F. Dias, G. Genty, and J. Dudley, "Caustics and rogue waves in an optical sea," Scientific Reports **5**, 12822 (2015).

[25] T. Pearcey, "XXXI. The structure of an electromagnetic field in the neighbourhood of a cusp of a caustic," The London, Edinburgh, and Dublin Philosophical Magazine and Journal of Science **37**, 311 (1946).

[26] M. Berry, "Waves and Thom's theorem," Advances in Physics **25**, 1 (1976).

[27] R. Borghi, "Evaluation of cuspoid and umbilic diffraction catastrophes of codimension four," Journal of the Optical Society of America A **28**, 887 (2011).

[28] R. Borghi, "Catastrophe optics of sharp-edge diffraction," Optics Letters **41**, 3114–3117 (2016).

[29] R. Borghi and C. Carosella, "Sharp-edge diffraction under Bessel beam illumination: a catastrophe optics perspective," Journal of the Optical Society of America A **39**, 1117–1127 (2022).

[30] J. Nye, "Optical caustics in the near field from liquid drops," Proceedings of the Royal Society of London A **361**, 21 (1978).

[31] M. Berry, J. Nye, and F. Wright, "The elliptic umbilic diffraction catastrophe," Philosophical Transactions of the Royal Society of London A **291**, 453 (1978).

[32] J. Nye, "The catastrophe optics of liquid drop lenses," Proceedings of the Royal Society of London A **1824**, 1 (1986).

[33] J. Nye, ""From Airy rings to the elliptic umbilic diffraction catastrophe," Journal of Optics A: Pure and Applied Optics **5**, 503 (2003).

[34] A. Zannotti, C. Denz, M. Alonso, and M. Dennis, "Shaping caustics into propagation-invariant light," Nature Communications **11**, 3597 (2020).

[35] A. Zannotti, F. Diebel, M. Boguslawski, and C. Denz, "Optical catastrophes of the swallowtail and butterfly beams," New Journal of Physics **19**, 053004 (2017).

[36] A. Zannotti, F. Diebel, and C. Denz, "Dynamics of the optical swallowtail catastrophe," Optica **4**, 1157–1162 (2017).

[37] H. Teng, Y. Qian, Y. Lan, and W. Cui, "Swallowtail-type diffraction catastrophe beams," Optics Express **29**, 3786–3794 (2021).

[38] M. Soskin, S. Boriskina, Y. Chong, M. Dennis, and A. Desyatnikov, "Singular optics and topological photonics," Journal of Optics **19**, 010401 (2017).

[39] A. Ferrando, ""Discrete-gauss states and the generation of focusing dark beams," Physical Review A **90**, 023844 (2014).

[40] J. Nye and M. Berry, "Dislocations in wave trains," Proceedings of the Royal Society of London A **336**, 165 (1974).

[41] M. Soskin and M. Vasnetsov, *"Singular optics" in Progress in optics, Volume 42*, edited by E. Wolf (North-Holland Publishing Company, Amsterdam, 2001).

[42] P. Coullet, L. Gil, and F. Rocca, "Optical vortices," Nature Physics **6**, 118 (2010).

[43] V. Bazhenov, M. Vasnetsov, and M. Soskin, "Laser beams with screw dislocations in their wavefronts," Optical and Quantum Electronics **24**, 951 (1990).

[44] A. Boivin and E. Wolf, "Electromagnetic field in the neighborhood of the focus of a coherent beam," Physical Review **138**, B1561–B1565 (1965).

[45] A. Boivin, J. Dow, and E. Wolf, "Energy Flow in the neighborhood of the focus of a coherent beam," Journal of the Optical Society of America **57**, 1171–1175 (1967).

[46] H. Rubinsztein-Dunlop and et al., "Roadmap on structured light," Journal of Optics **19**, 013001 (2017).

[47] Y. Shen, X. Wang, Z. Xie, C. Min, X. Fu, Q. Liu, M. Gong, and X. Yuan, "Optical vortices 30 years on: OAM manipulation from topological charge to multiple singularities," Light: Science & Applications **8** (2019), 10.1038/s41377-019-0194-2.

[48] M. Dennis, Y. Kivshar, M. Soskin, and G. Swartzlander Jr, "Singular Optics: more ado about nothing," Journal of Optics A: Pure and Applied Optics **11**, 090201 (2009).

[49] A. Desyatnikov, L. Torner, and Y. Kivshar, *"Optical Vortices and Vortex Solitons" in Progress in optics, Volume 47*, edited by E. Wolf (Cambridge University Press, Cambridge, 1999).

[50] A. Askin, "Acceleration and trapping of particles by radiation pressure," Physical Review Letters **24**, 156–159 (1970).

[51] K. Dholakia and T. Cizmar, "Shaping the future of manipulation," Nature Photonics **5**, 335 (2011).

[52] M. Padgett and R. Bowman, "Tweezers with a twist," Nature Photonics **5**, 343 (2011).

[53] M. Berry and M. Dennis, "Knotting and unknotting of phase singularities: Helmholtz waves, paraxial waves and waves in 2 + 1 spacetime," Journal of Physics A: Mathematical and general **34**, 8877 (2001).

[54] M. Dennis, R. King, B. Jack, K. O'Holleran, and M. Padgett, "Isolated optical vortex knots," Nature Physics **6**, 118 (2010).

[55] A. Desyatnikov, D. Buccoliero, M. Dennis, and Y. Kivshar, "Suppression of Collapse for spiraling elliptic solitons," Physical Review Letters **104**, 053902 (2010).

[56] A. Desyatnikov, D. Buccoliero, M. Dennis, and Y. Kivshar, "Spontaneous knotting of self-trapped waves," Scientific Reports **2**, 771 (2012).

[57] W. Thomson, "On vortex atoms," Proceedings of the Royal Society of Edinburgh **6**, 94 (1869).

[58] H. Helmholtz, "LXIII. On Integrals of the hydrodynamical equations, which express vortex-motion," The London, Edinburgh, Dublin Philosophy Magazine and Journal of Science **33**, 485 (1867).

[59] D. Akhmetov, *Vortex Rings* (Springer, Berlin, Heidelberg, 2009).

[60] C. Barenghi and R. Donnelly, "Vortex rings in classical and quantum systems," Fluid Dynamics Research **41**, 051401 (2009).

[61] G. Airy, "On the diffraction of an object-glass with circular aperture," Transactions of the Cambridge Philosophical Society **5**, 283 (1835).

[62] M. Berry and M. Dennis, "Knotted and linked phase singularities in monochromatic waves," Proceedings of the Royal Society of London A **457**, 2251 (2001).

[63] J. Ruostekoski and Z. Dutton, "Engineering vortex rings and systems for controlled studies of vortex interactions in Bose-Einstein condensates," Physical Review A **72**, 063626 (2005).

[64] A. Desyatnikov, "Vortex rings in paraxial laser beams," optics Express **31**, 31955 (2023).

[65] M. Berry and M. Dennis, "Topological events on wave dislocation lines: birth and death of loops, and reconnection," Journal of Physics A **40**, 65 (2007).

[66] G. P. Karman, M. W. Beijersbergen, A. van Duijl, and J. P. Woerdman, "Creation and annihilation of phase singularities in a focal field," Optics Letters **22**, 1503 (1997).

[67] Z. Kulchukova and A. Desyatnikov, "Vortex ring reconnections in elliptic Gaussian beams," Optics Letters **49**, 915 (2024).

[68] J. Nye, "Unfolding of higher-order wave dislocations," Journal of the Optical Society of America A **15**, 1132 (1998).

[69] J. Nye, "Dislocation lines in the swallowtail diffraction catastrophe," Proceedings of the Royal Society of London A **463**, 343–355 (2007).

[70] J. Nye, "Unfolding higher-order wave dislocation clusters and catastrophe theory," Journal of Optics A: Pure and Applied Optics **10**, 075010 (2008).

[71] M. Bandres and J. Gutierrez-Vega, "Ince Gaussian beams," Optics Letters **29**, 144–146 (2004).

[72] K. Tschernig, D. Guacaneme, O. Mhibik, I. Divliansky, and M. Bandres, "Observation of Boyer-Wolf Gaussian modes," Nature Communications **15**, 5301 (2024).

[73] E. Karimi, G. Zitoand, B. Piccirillo, L. Marrucci, and E. Santamato, "Hypergeometric-Gaussian beam," Optics Letters **32**, 3053–3055 (2007).